Non-geometric tilt-to-length coupling in precision interferometry: mechanisms and analytical descriptions

Marie-Sophie Hartig, Sönke Schuster, Gerhard Heinzel, and Gudrun Wanner

Max Planck Institute for Gravitational Physics (Albert Einstein Institute) and Institute for Gravitational Physics of the Leibniz Universität Hannover, Callinstrasse 38, 30165 Hannover, Germany

E-mail: marie-sophie.hartig@aei.mpg.de, gudrun.wanner@aei.mpg.de

July 2022

Abstract. This paper is the second in a set of two investigating tilt-to-length (TTL) coupling. TTL describes the cross-coupling of angular or lateral jitter into an interferometric phase signal and is an important noise source in precision interferometers, including space gravitational wave detectors like LISA. We discussed in [1] the TTL coupling effects originating from optical path length changes, i.e. geometric TTL coupling. Within this work, we focus on the wavefront and detector geometry dependent TTL coupling, called non-geometric TTL coupling, in the case of two interfering fundamental Gaussian beams. We characterise the coupling originating from the properties of the interfering beams, i.e. their absolute and relative angle at the detector, their relative offset and the individual beam parameters. Furthermore, we discuss the dependency of the TTL coupling on the geometry of the detecting photodiode. Wherever possible, we provide analytical expressions for the expected TTL coupling effects. We investigate the non-geometric coupling effects originating from beam walk due to the angular or lateral jitter of a mirror or a receiving system. These effects are directly compared with the corresponding detected optical path length changes in [1]. Both together provide the total interferometric readout. We discuss in which cases the geometric and non-geometric TTL effects cancel one-another. Additionally, we list linear TTL contributions that can be used to counteract other TTL effects. Altogether, our results provide key knowledge to minimise the total TTL coupling noise in experiments by design or realignment.

Keywords: tilt-to-length coupling, optical cross-talk, wavefront properties, interferometric noise sources, laser interferometry, space interferometry, LISA

1. Introduction

Tilt-to-Length (TTL) coupling is a common type of noise in precision laser interferometers. It describes the unwanted coupling of angular or lateral jitter into the phase readout. Within this paper, the jittering object can either be a reflective

component or a receiving system, i.e. an optical bench or a satellite that is receiving the beam of interest. The TTL coupling from a jittering transmitter is not discussed here.

In general, TTL coupling originates, on the one hand, from the fact that the optical distance along the beam axis is lengthened or shortened by the jitter. This results in changes of the optical path length difference (OPD) of the beam axis and has been discussed in detail in [1]. On the other hand, the jitter changes the interference pattern. These changes depend on the wavefront properties and originate from alterations in the beam alignment with respect to the detector surface and with respect to each other. Additionally, beam displacements on the detector surface can result in beam clipping by the boundaries of the detector surface. All these effects contribute to the final interferometric output signal. After all, an interferometer does not directly sense an OPD but rather a phase difference on the detector surface. This is typically converted to a length readout signal, the longitudinal path length sensing (LPS) signal, by dividing the phase by the wavenumber k [2, 3]. We categorise these LPS changes as non-geometric effects.

Although it is often sufficient to focus on the geometric TTL effects, there are cases where the non-geometric TTL effects become equal or even dominant noise contributors. One example of this are setups in which the centre of rotation is located in the beam's point of incidence on the detector, which results in the suppression of the geometric coupling effects. This is implemented in the LISA mission [4, 5] by imaging systems [6, 2] reducing the geometric jitter coupling of the receiving spacecraft. Another important example of dominant non-geometric coupling is the TTL coupling of the jitter of a transmitting spacecraft in the LISA mission into the long arm interferometer readout, computed, for instance, in [7, 8, 9], which we do not consider in this work. More general examples that are independent of a specific mission have been introduced in [1, 3, 10], and are further discussed within this paper.

TTL coupling has been investigated for different missions in various publications. It is discussed for the LISA long arm interferometer in [2, 7, 8, 9], for the LISA test mass interferometer in [11], and for the GRACE-FO mission in [12], and for the LISA Pathfinder mission in [13, 14, 15, 16]. Here, we provide a very general overview of non-geometric TTL effects applicable to precision interferometers, including space interferometers. The work presented here is fundamental and not limited to a dedicated mission or project.

Within this work, we focus on the local interferometric effects and assume fundamental Gaussian beams. We briefly repeat in Sec. 2 the mechanisms inducing TTL coupling with focus on the resulting shift of a laser beam's point of incidence at the detector surface. This beam walk on the detector changes the interference pattern and, therefore, couples into the signal. The non-geometric coupling effects are then described analytically in Sec. 3. In particular, we categorise the non-geometric TTL effects into linear, quadratic or mixed effects. We divide our analysis into the investigation of wavefront and detector related coupling effects. We summarise all non-geometric effects

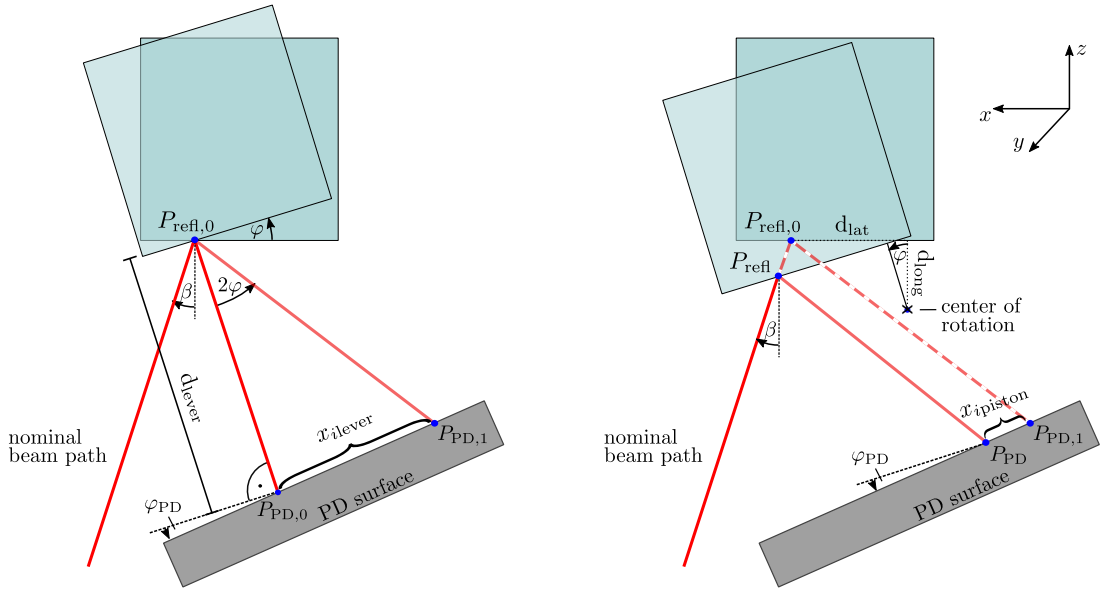

Figure 1. Beam walk induced by two TTL mechanisms in the case of mirror rotations. Left figure: The lever arm mechanism. Shown is the displacement $x_{i\mathrm{lever}}$ of the point of incidence from $P_{\mathrm{PD},0}$ to $P_{\mathrm{PD},1}$ due to a tilt φ of the mirror around the reflection point $P_{\mathrm{refl},0}$. The displacement scales with the distance d_{lever} of the photodiode (PD) from the mirror, which is defined along the nominal beam axis (case $\varphi = 0$). Right figure: The piston mechanism. The centre of rotation is shifted with respect to the reflection point (longitudinally by d_{long} and laterally by d_{lat}, both are positive here). This causes a beam walk $x_{i\mathrm{piston}}$ from point $P_{\mathrm{PD},1}$ to point P_{PD} additionally to the lever arm beam walk. The dashed line corresponds to the beam path due to the lever arm effect. In both figures, β marks the beam's angle of incidence at the mirror and φ_{PD} denotes the rotation of the PD surface with respect to the nominal beam axis. Arrows pointing clockwise indicate negative angles.

in Sec. 4 and list them for a typical special case. In Sec. 5, we extend this summary to the full LPS signal. There, we combine the results from [1] and this work to discuss the total signal. Finally we give a conclusion in Sec. 6.

2. Non-geometric TTL coupling in different systems

TTL coupling occurs in different types of precision interferometer. We group these interferometers in two different categories, just as described in [1]. The first category of interferometers comprises systems where the TTL originates from an angularly or laterally jittering mirror. Most laboratory systems, as well as the LISA Pathfinder interferometers [17, 13, 16] and LISA test mass interferometer [4, 5] fall into this category. The second category covers systems, where the TTL originates from the jitter of a system relative to a static beam. This occurs, for instance, if a spacecraft is jittering relative to the laser beam it is receiving from a far spacecraft, like in the GRACE-FO mission [18, 19] and in the LISA long-arm interferometers [4, 5].

We now assume a mirror that is subject to angular jitter. As one can see on

the left-hand side of Fig. 1, the path along which the reflected beam propagates to the photodiode is then angle-dependent and deviates from the nominal path, i.e. the path for $\varphi = 0$. This affects the optical path length (OPL) of the beam axis but also the point of incidence at the detector, i.e. the point at which the beam axis hits the photodiode surface. We refer to this behaviour as 'beam walk' since the beam's point of incidence walks along the surface for increasing tilt angles. Like the angular alignment of the interfering beams at the detector, the offset between both points of incidence significantly affects the interference pattern. Correspondingly, the beam walk is an important contributor to the entire non-geometric TTL coupling. The beam walk depicted in Fig. 1 originates from two different mechanisms: the lever arm and the piston mechanism. The changes of the beam axis lengths due to these mechanisms have separately been discussed in [1].

The lever arm mechanism (left-hand side of Fig. 1) describes the angular jitter of a mirror surface around the beam reflection point $P_{\mathrm{refl,0}}$. The beam then follows the light red path and hits the detector in an angle-dependent point $P_{\mathrm{PD,1}}$. The distance $x_{i\mathrm{lever}}$ between the original point of incidence $P_{\mathrm{PD,0}}$ and $P_{\mathrm{PD,1}}$ describes the lever arm induced beam walk. The change caused by this beam walk in the LPS signal is the non-geometric lever arm effect.

The piston mechanism (right-hand side of Fig. 1) describes all additional beam path changes originating from a displacement of the mirror's centre of rotation with respect to the reflection point. In that case, the mirror surface would shift in or out of the beam path, which simultaneously shifts the reflection point from $P_{\mathrm{refl,0}}$ to P_{PD} and the beam's point of incidence at the detector from $P_{\mathrm{PD,1}}$ to point P_{PD}. The LPS signal change caused by the beam walk on the photodiode is the non-geometric piston effect.

Let us now consider the second category of interferometers with an angularly jittering receiving system. There, a jittering optical bench receives a static beam which is then incident on a photodiode that jitters together with the optical bench and all other components in the system. Thereby, the detector surface moves into or out of the received beam, which alters the optical path length and, thereby, introduces geometric TTL coupling. Simultaneously it changes the wavefront properties on the photodiode and causes beam walk, which again results in non-geometric TTL coupling. The beam walk is illustrated in Fig. 2, where $P_{\mathrm{PD,0}}$ was the the nominal point of incidence, while the beam impinges in point $P_{\mathrm{PD,1}}$ if the system is rotated by φ_{RS}.

The non-geometric TTL coupling of both a jittering mirror and a jittering receiver are discussed in detail in the following.

3. Non-geometric TTL coupling effects

There are different aspects that affect the non-geometric TTL coupling. We systematically analyse these aspects within this section. We start by introducing the LPS signal in detail and discuss why and how it deviates from the OPD (Sec. 3.1). In Sec. 3.2 we derive non-geometric TTL effects that relate to the properties of the

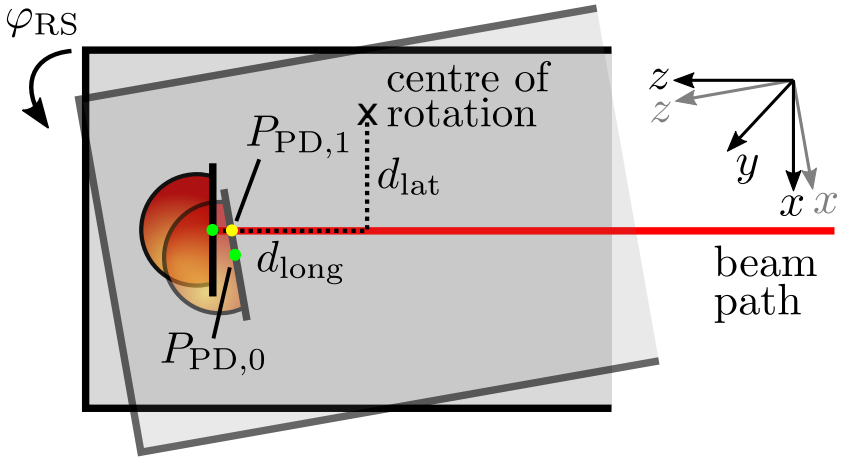

Figure 2. TTL coupling due to angular jitter of the system (grey open box) with respect to the incoming beam (red trace). The geometric TTL effect is visible by the distance change along the beam axis when the photodiode (PD) moves into the received beam. Non-geometric effects occur, for instance, due to the change of the beam's incidence point on the detector, which moves from the green point in the centre of the diode, to a yellow point $P_{\mathrm{PD},1}$ shifted from this centre. The distances d_{long} and d_{lat} define the longitudinal and lateral distances between the nominal point of incidence $P_{\mathrm{PD},0}$ and the centre of rotation. Both are positive in this figure.

interfering wavefronts. Finally, we discuss in Sec. 3.3 effects that relate to the detector geometry, i.e. whether, for instance, a large single element photodiode is used or a small quadrant photodiode.

3.1. Introduction: LPS and OPD

Throughout this paper, we are assuming the case of interfering Gaussian beams, which can be described according to [3] by

$$E(r_b, z_b, t) \propto \frac{1}{w(z_b)} \exp\left(\frac{-r_b^2}{w^2(z_b)}\right) \cdot \exp\left(i\Omega t - i\left[\frac{k r_b^2}{2R(z_b)} - \eta(z_b) + k\,\mathrm{OPL}_b\right]\right) , \tag{1}$$

where all variable definitions are listed in Tab. 1. The lower index b of Eq. (1) stands for 'beam' and is, therefore, substituted in Tab. 1 by either m or r referring to a measurement or reference beam respectively. The measurement beam is the beam of interest that either reflects from the mirror in the case of a jittering mirror or is received from a distant optical bench in the case of a jittering receiving system. This beam interferes with a second beam, the reference beam, on the detector. This reference beam is assumed to be static with respect to the detector surface.

For two interfering beams, the detected power can be derived via the integral of the squared absolute sum of their electric fields over the photodiode surface S:

$$P \propto \int dS\, \|E_m + E_r\|^2 \tag{2}$$

Table 1. List of physical parameters.

parameter	description	characterising eq.
k	wave number common for both beams	$k = 2\pi/\lambda$
λ	wavelength	
$\Omega_{m,r}$	angular frequency of meas. / ref. beam	$\Omega = ck = 2\pi f$
$\Delta\Omega$	angular heterodyne frequency	$\Delta\Omega = \lvert\Omega_m - \Omega_r\rvert$
$z_{R,m,r}$	Rayleigh range of meas. / ref. beam	$z_R = \pi\, w_0^2/\lambda$
$w_{0,m,r}$	waist size of meas. / ref. beam	$w_0 = \sqrt{z_R\,\lambda/\pi}$
$w_{m,r}$	laser spot size on detector	$w = w_0\sqrt{1 + (z/z_R)^2}$
$R_{m,r}$	radius of curvature of meas. / ref. beam	$R = z\,(1 + (z_R/z)^2)$
$\eta_{m,r}$	Gouy phase of meas. / ref. beam	$\eta = \arctan(z/z_R)$
$P_{m,r}$	power of meas. / ref. beam	
$z_{m,r}$	distance from waist in direction of propagation for meas. / ref. beam	
$s_{m,r}$	propagation distance of meas. / ref. beam	
$r_{m,r}$	cylindrical coordinate of meas. / ref. beam	$r = \sqrt{x^2 + y^2}$

$$= \int dS\ \left(\|E_m\|^2 + \|E_r\|^2 + E_m E_r^* + E_m^* E_r\right)\,. \tag{3}$$

The first two summands describe the detected power of the individual beams. The third and the forth summand, evaluated for $t = 0$, are often referred to as complex amplitudes a of the beat note. The argument of this complex amplitude is then the interferometric phase ϕ [3], e.g.

$$\phi = \arg(a) = \arg\left(\int dS\ E_m E_r^*|_{t=0}\right)\,, \tag{4}$$

sensed by the corresponding interferometric readout system. This description is equally valid for homodyne and heterodyne interferometers.

The longitudinal path length sensing (LPS) signal is this phase converted to a length by a division by the wavenumber k:

$$\mathrm{LPS} = \frac{1}{k}\,\phi\,. \tag{5}$$

This derivation is valid if the entire interference pattern is detected with homogenous sensitivity, so for single element photodiodes (SEPDs), which are sufficiently large to detect the complete incident wavefronts. We will extend this for quadrant photodiodes (QPDs) in Sec. 3.3.

The LPS represents the actual displacement measurement of interferometers. However, it is more complicated to compute both numerically and analytically than the OPD. The OPD, on the other hand, can be derived from simple geometry but gives only information along the beam axis. Because each OPL is defined along the corresponding beam axis, the OPD is (approximately) constant in the surface integral of Eq. (4). It can therefore be drawn out of this integral:

$$\phi = \arg\Big[\exp(-ik(\mathrm{OPL}_m - \mathrm{OPL}_r)) \cdot$$

$$\left(\int dS(E_m E_r^*)|_{\mathrm{OPL}_{m,r}=t=0} \right) \Big] \tag{6}$$

$$= \arg\left[\exp(ik\,\mathrm{OPD}) \left(\int dS(E_m E_r^*)|_{\mathrm{OPL}_{m,r}=t=0} \right) \right] \tag{7}$$

$$= k\,\mathrm{OPD} + \arg\left[\left(\int dS(E_m E_r^*)|_{\mathrm{OPL}_{m,r}=t=0} \right) \right]. \tag{8}$$

Strictly speaking, this derivation only holds for beams of normal incidence. In the case of tilted beams, an additional microscopic phase needs to be considered when the OPD is taken out of the integral [3]. Yet, the OPD can be separated in either case from the non-geometric phase (second summand in Eq. (8)). Thus, the LPS can be split into the OPD and a non-geometric contribution $\mathrm{LPS}_{\mathrm{ng}}$:

$$\mathrm{LPS} = \mathrm{OPD} + \mathrm{LPS}_{\mathrm{ng}}\,. \tag{9}$$

The non-geometric part $\mathrm{LPS}_{\mathrm{ng}}$ contains then all contributions related to the wavefront properties (i.e. the involved radii of curvature R_b, Gouy phases η_b and spot sizes w_b). Additionally, it contains clipping effects if the detector surface S is not large enough to receive the full extent of the impinging wavefronts. A more detailed description about the numerical implementation of these equations and possibly needed coordinate transformation is given in [3]. The LPS signal measured in a laboratory experiment includes additional effects that are not included in the presented equations, such as from the non-uniformity of the photodiode's responsivity.

3.1.1. Derivation of LPS_{ng} in analytical and in numerical simulations In numerical simulations that allow both a computation of the LPS as well as the OPD (this is for instance the case in IfoCAD [3, 20]), one can naturally derive the $\mathrm{LPS}_{\mathrm{ng}}$ simply from the difference

$$\mathrm{LPS}_{\mathrm{ng}} = \mathrm{LPS} - \mathrm{OPD}\,. \tag{10}$$

In analytical derivations, this process would be significantly more complex than necessary. In the analytic and numeric approach, the OPD can be derived as described in [1] via the difference between the OPLs of the measurement beam in the tilted and the nominal case. However, the computation of the non-geometric TTL contributions can be simplified by adapting the simulation to directly exclude OPL changes and making them zero by design. In that case, the LPS signal in Eq. (10) is fully non-geometric and can be derived analytically using the procedure described in [21] summarised in the following:

To account for the tilt angle of each of the beams b and the rotation axis defining a rotation matrix $M_{\mathrm{rot},b}$, as well as the location of the centre of rotation $\mathbf{p}_{\mathrm{pivot},b}$, we first perform a coordinate transformation in Eq. (1). The new coordinates are defined with respect to the photodiode centre, i.e. $z = 0$.

$$\begin{pmatrix} x_b \\ y_b \\ \Delta\mathrm{OPL}_b \end{pmatrix} = M_{\mathrm{rot},b} \left[\begin{pmatrix} x_b \\ y_b \\ 0 \end{pmatrix} - \mathbf{p}_{\mathrm{pivot},b} \right] + \left[\mathbf{p}_{\mathrm{pivot},b} - \begin{pmatrix} x_{i,b} \\ y_{i,b} \\ 0 \end{pmatrix} \right] \tag{11}$$

The beams are then superimposed on the photodiode, and the overlap integral in Eq. (4) and the resulting LPS signals are analytically evaluated. In the analytical evaluation of the overlap integral, it is assumed that the beam parameters do not vary for different detector points. This simplifying assumption is not necessary in numerical computations using IfoCAD.

For the computation of the non-geometric signal contribution only, we substitute the pivot point $\mathbf{p}_{\mathrm{pivot},b}$ by the beam's point of incidence $(x_{\mathrm{im}}, y_{\mathrm{im}}, 0)$ on the photodiode surface. By this replacement, all OPD contributions become zero and, therefore, $\mathrm{LPS} = \mathrm{LPS}_{\mathrm{ng}}$.

Note, that for cases where the pivot is not actually on the detector, a beam walk occurs on the photodiode. That means, the incidence point $(x_{\mathrm{im}}, y_{\mathrm{im}})$ varies during the rotation, i.e. it is angle-dependent. This angular dependency will be taken into account in the computation of $\mathrm{LPS}_{\mathrm{ng}}$ when the pivot is set to be on the diode. We will show this in more detail below in Sec. 3.2.2.

In general, we reduce the complexity of the analytic equations by neglecting the angular dependency of beam parameters as a higher-order contribution.

We have used this procedure for the derivation of all $\mathrm{LPS}_{\mathrm{ng}}$ equations below.

3.2. Wavefront related TTL coupling effects: case of ideal detectors

The interferometric phase depends on the one hand on the beam properties (integrand in Eq. (4)) and on the other hand on the detector geometry (domain of integration in Eq. (4)). In this section, we investigate how the beam properties, i.e. their beam parameters, affect the phase signal and show how this wavefront dependent TTL coupling depends on the point of incidence at the detector. To differentiate between the wavefront related TTL effects discussed in this section and the detector related TTL effects that are discussed in Sec. 3.3, we assume in our analytic investigations here that the detectors are ideal infinitely large single element photodiodes (SEPD).

We start with analysing the TTL coupling in the most simplified setup of two perfectly identical fundamental Gaussian beams and the measurement beam rotating around its point of incidence on the detector. We distinguish the case where the beams overlap perfectly (Sec. 3.2.1) and the case of a laterally shifted measurement beam Sec. 3.2.2. This is extended in Sec. 3.2.3 for rotations around an arbitrary point, thus including a beam walk on the detector. Such a beam walk potentially breaks the symmetry between the wavefronts of the incoming beams and thereby affects the TTL coupling. We therefore also investigate the TTL coupling induced by the beam walk due to mirror rotations (Sec. 3.2.4). Additionally, refractions of angularly jittering beams at transmissive components leads to a changing beam walk (Sec. 3.2.5). Since identical Gaussian beams are idealisations impossible to achieve in reality, we further discuss TTL effects induced by beams having unequal beam parameters in Sec. 3.2.6. Any deviation from the wavefront or intensity shape will alter the balance between wavefronts and thus generate cross-coupling. This is discussed in Sec. 3.2.7.

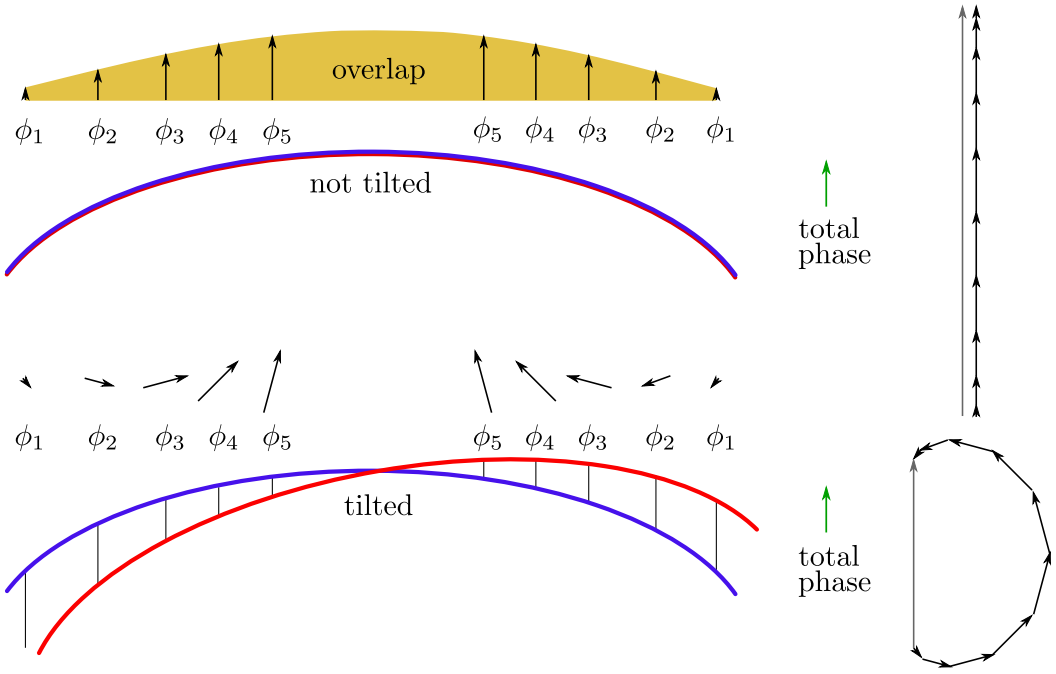

Figure 3. Simplified illustration for the vanishing TTL in case of identical Gaussian beams rotating around their joint point of incidence on the photodiode. Shown are the superposition of two wavefronts in the nominal untilted case (upper sketch with superimposing blue and red wavefronts) and the case when the measurement wavefront is tilted around the centre of the reference wavefront (lower sketch). The local phase differences between the wavefronts are indicated by ϕ_i and are illustrated by the directions of the black arrows (vector representations of the local complex amplitudes). The phase information at different positions on the detector is weighted with the amplitude of the total field ("overlap") resulting from the superposition of the two interfering beams. The phase sum ϕ_{sum} represents the integrated phase over the entire detector. This ϕ_{sum} is indicated by the direction of the green arrows on the right-hand side. Due to the given symmetry, ϕ_{sum} is unaffected by the rotation, which shows that there is no non-geometric TTL, i.e. $\text{LPS}_{\text{ng}} = 0$.

3.2.1. Identical Gaussian beams rotating around an identical point of incidence on PD
We now assume the most simple case of two identical fundamental Gaussian beams rotating around an identical point of incidence. For a rotation angle of $\varphi_m = 0$ both beams and beam paths are identical and they perfectly overlap each other. In the following, the measurement beam gets rotated around its shared incidence point on the detector. The beam's geometric path length does not change, giving here a pure non-geometric path length readout.

In the following, we will derive the TTL coupling in this particular case first qualitatively via a graphic and then analytically.

The graphical derivation of TTL coupling is based on an approximation of Eq. (4). In the process, we estimate the resulting phase visually from graphical illustrations. We start with the mathematical background of this approach. Therefore, we first divide the surface integral in Eq. (4) into n segments S_i. The complex amplitude a then equals

the sum over the complex amplitudes a_i of the segments S_i

$$a = \sum_{i=1}^{n} a_i \tag{12}$$

$$a_i \propto \int dS_i (E_m E_r^*)|_{t=0} \, . \tag{13}$$

The expected interferometric phase ϕ is then given by the argument of the sum of all complex amplitudes:

$$\phi = \arg(a) = \arg\left(\sum_{i=1}^{n} a_i\right) \, . \tag{14}$$

In our graphical approach, we examine a small number of complex amplitudes a_i visually from the differences of the interfering wavefronts. This is illustrated in Fig. 3 showing the wavefronts of two interfering beams in the nominal non-tilted case and for an arbitrarily chosen tilt angle φ_m. Here, the vector representations of the complex valued amplitudes a_i are given by the black arrows. Their directions define the local phase differences ϕ_i. In the figure, these are estimated from the difference (averaged difference within a certain segment) of the phase profiles, i.e. the blue and red wavefronts. Further, the lengths of the arrows are defined by the Gaussian amplitude profile of the interference pattern, qualitatively described by the yellow area. In accordance to Eq. (14), the full complex amplitude equals the sum of the black arrows. The interferometric phase ϕ then equals the angle of this vector sum.

We now evaluate the total phases for the case shown in Fig. 3: While the local phase differences are all zero in the no-tilted case, a tilt of the measurement beam (red wavefront) changes the directions but not the lengths of the complex amplitude vectors. Due to the given symmetry, the arrows on the right- and left-hand sides are antisymmetric, which results again in a total phase of zero, i.e. the same value as in the non-tilted case, showing that no TTL coupling will occur.

We confirm this graphical derivation by deriving the LPS signal analytically using the methods described in [3, 21]. Therefore, we evaluate Eq. (4) for the electrical fields of identical Gaussian beams, i.e. beams with the same Rayleigh ranges $z_{Rm} = z_{Rr}$, distances from waist $z_m = z_r$ and incidence points $x_{im} = x_{ir}$ at the detector. For small beam tilts φ_m we find

$$\mathrm{LPS}_{\mathrm{ng}}^{\mathrm{SEPD,2D}} \approx -\frac{z_m}{4k\, z_{Rm}} \left(\varphi_m^2 - 2\varphi_m \varphi_{\mathrm{PD}}\right) \tag{15}$$

which corresponds to results from [10] but additionally describes the contribution of a small tilt φ_{PD} of the detector surface.

The term we find in the analytical derivation is assumed to originate from the simplifying assumptions made in the computation of the LPS signal (see Sec. 3.1.1). However, Eq. (15) evaluates as numerical zero for small photodiode tilts $|\varphi_{\mathrm{PD}}| \lesssim 200\,\mu\mathrm{rad}$ and common parameters, e.g. $|\varphi_m| \lesssim 200\,\mu\mathrm{rad}$, $\lambda = 1064\,\mathrm{nm}$, $z_m \sim 1\,\mathrm{m}$, $z_{Rm} \sim 1\,\mathrm{m}$. Thus we can conclude that there would be no TTL coupling in the case of two identical Gaussian beams with one rotating around the shared point of incidence.

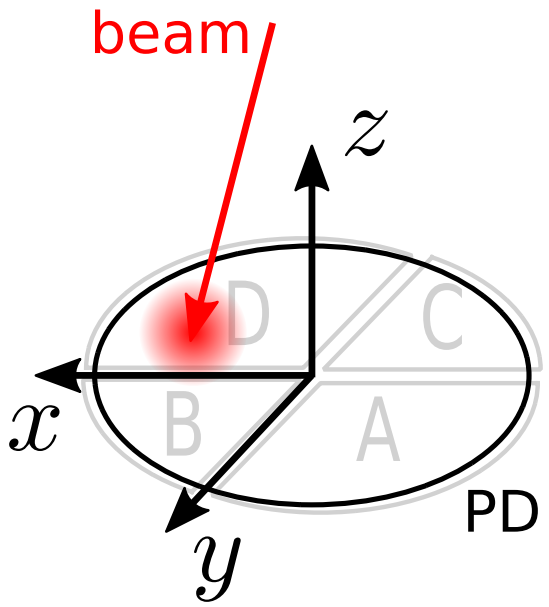

Figure 4. Coordinate system of a single element (black circle) or quadrant (grey quarter circles) photodiode, respectively. The four quadrants of the quadrant photodiode are labelled A, B, C and D.

3.2.2. Laterally shifted identical Gaussian beams By assuming a perfect overlap of both interfering beams for $\varphi_m = 0$ as well as a centre of rotation positioned exactly at the point of incidence, we considered a very special case in Sec. 3.2.1. We now relax these conditions step-wise. Within this subsection, we investigate how the TTL coupling changes if the two beams are laterally shifted with respect to each other. Let x_{im}, x_{ir} describe the beams' points of incidence with respect to a hypothetical centre of the infinitely large SEPD (see Fig. 4 for the coordinate system). The measurement beam's centre of rotation is now placed in this new point, i.e. it jitters angularly around the point defined by x_{im}.

While without beam offsets, the amplitude of the overlap is symmetric with respect to the wavefronts, the symmetry axes of the overlap and the interfering beams differ from each other once offsets of the detection points are introduced. An offset of one beam and the resulting imbalance of the overlap will favour one side and thus generate cross-coupling, as demonstrated in Fig. 5.

We compute this case again analytically as described in 3.2.1 and find

$$\begin{aligned} \mathrm{LPS}_{\mathrm{ng}}^{\mathrm{SEPD,2D}} \approx & \frac{1}{2}(x_{im} - x_{ir})\left[(\varphi_m - \varphi_{\mathrm{PD}}) + (\varphi_r - \varphi_{\mathrm{PD}})\right] \\ & + \left[(x_{im} - x_{ir})^2 \frac{z_m}{8 z_{Rm}^2} - \frac{z_m}{4k\, z_{Rm}}\right]\left(\varphi_m^2 - 2\varphi_m\varphi_{\mathrm{PD}}\right) \end{aligned} \tag{16}$$

or in a three-dimensional case neglecting detector angles

$$\begin{aligned} \mathrm{LPS}_{\mathrm{ng}}^{\mathrm{SEPD,3D}} \approx & \frac{1}{2}(x_{im} - x_{ir})(\varphi_m + \varphi_r) \\ & - \frac{1}{2}(y_{im} - y_{ir})(\eta_m + \eta_r) \end{aligned}$$

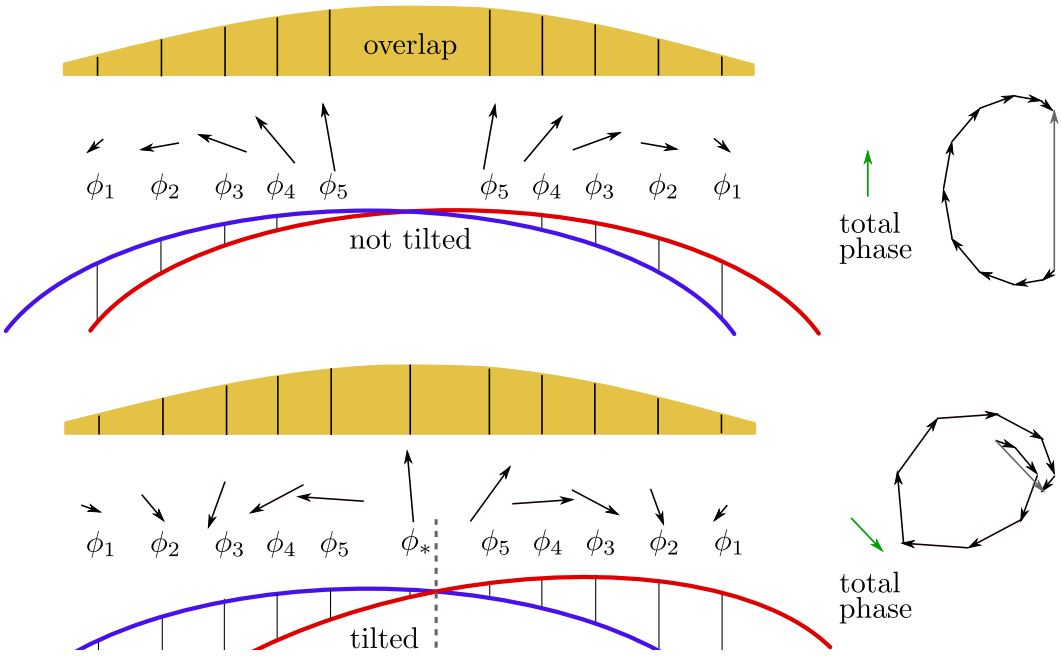

Figure 5. TTL coupling for a laterally shifted measurement beam (red), which rotates around its incidence point on the photodiode. The phase information at different positions on the detector is weighted with the overlap (product of the electric field amplitudes) between the two interfering beams. For non-tilted beams, the local phase differences cancel in the total phase (i.e. the green arrow points upwards). For a tilted measurement beam, this is no longer the case (i.e. the green arrow is rotated): the pairs of local phase differences ϕ_i, $i \in \{1, ..., 5\}$ distributed around the symmetry axis of the amplitude profile do not cancel each other. Consequently, the total phase changes, i.e. the sum of the paired local phase differences ϕ_i and the non-zero phase difference at the symmetry point of the amplitude profile at the photodiode surface ϕ_* is different than in the non-tilted case. This is caused by a displacement of the symmetry axis (dashed grey line) of the differential wavefront (indicated by the vertical lines between the blue and red wavefront) with respect to the symmetry axis of the amplitude profile of the total field.

$$
\begin{aligned}
&+ \left[(x_{im} - x_{ir})^2 \frac{z_m}{8 z_{Rm}^2} - \frac{z_m}{4k\, z_{Rm}} \right] \varphi_m^2 \\
&+ \left[(y_{im} - y_{ir})^2 \frac{z_m}{8 z_{Rm}^2} - \frac{z_m}{4k\, z_{Rm}} \right] \eta_m^2 \\
&- \frac{z_m}{z_{Rm}^2 + z_m^2}\, x_{im} y_{im}\, \varphi_m \eta_m \,. \qquad (17)
\end{aligned}
$$

Here, y_{im}, y_{ir} denote the vertical displacement of the points of incidence with respect to the hypothetical centre of the photodiode, and η_m the measurement beam's pitch angle. Both equations, Eq. (16) and Eq. (17), are series expanded up to second-order in all angles. In this expansion, we neglected all constant second-order angles (i.e. $(\varphi_r - \varphi_{\mathrm{PD}})^2$ and φ_{PD}^2) but kept all linear constants in preparation for Sec. 3.2.3 and Sec. 3.2.4.

As previously discussed in Sec. 3.2.1, the terms in Eqs. (16) and (17) which include a division by the wavenumber k are negligible. The same applies in usual laboratory

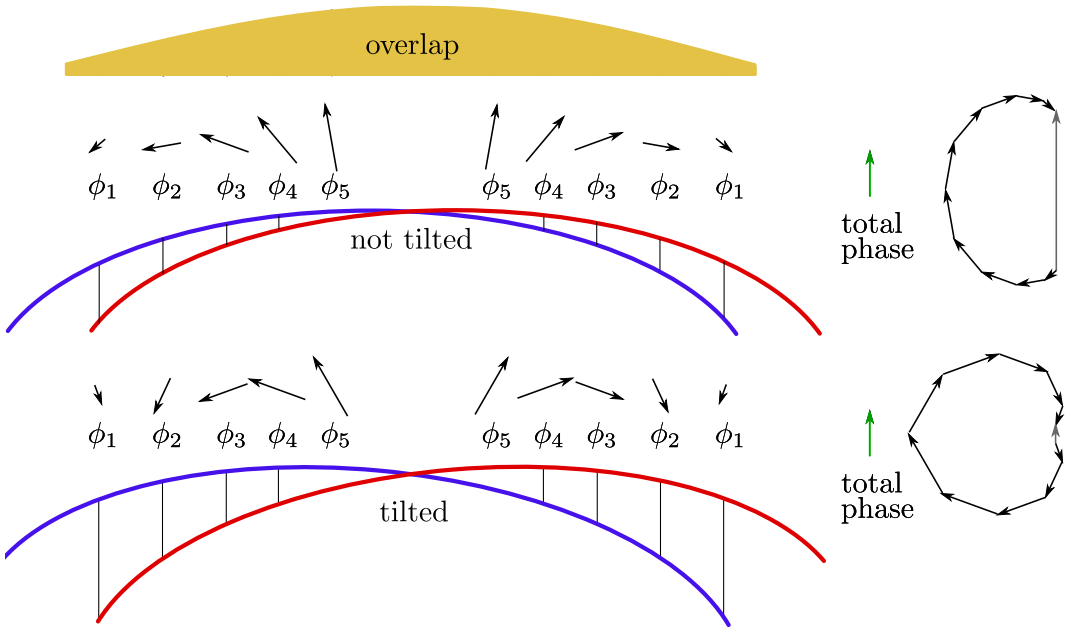

Figure 6. For two beams that are shifted with respect to each other and are rotated by the same angle but in opposite directions, i.e. $\varphi_m = -\varphi_r$, the amplitude profile is symmetric and the local phase differences cancel each other.

setups for the terms with quadratic offsets between the points of incidence on the detector because commonly used photodiodes are small and so are the spot sizes of the interfering beams. To find a high contrast of the signal, $x_{im} - x_{ir}$ must, therefore, be small, i.e. at most of the order of 10^{-5} m. We can, therefore, usually reduce Eqs. (16) and (17) to

$$\mathrm{LPS}_{\mathrm{ng}}^{\mathrm{SEPD,2D}} \approx \left[\frac{1}{2}(x_{im} - x_{ir})\right] [(\varphi_m - \varphi_{\mathrm{PD}}) + (\varphi_r - \varphi_{\mathrm{PD}})] \tag{18}$$

$$\begin{aligned}\mathrm{LPS}_{\mathrm{ng}}^{\mathrm{SEPD,3D}} \approx\ & \frac{1}{2}(x_{im} - x_{ir})(\varphi_m + \varphi_r) \\ & - \frac{1}{2}(y_{im} - y_{ir})(\eta_m + \eta_r)\,.\end{aligned} \tag{19}$$

It follows from Eq. (18) that we would measure no TTL coupling if the measurement and the reference beam are tilted by inverse angles, i.e. $\varphi_m = -\varphi_r$, and $\varphi_{\mathrm{PD}} = 0$. This cancellation of the signal in the case of inverse angles is illustrated in Fig. 6. This shows that not the differential but the absolute alignment of both beams couples into the signal.

Finally, taking into account both x_{im} and y_{im} are constant, we simplify Eq. (19) to

$$\mathrm{LPS}_{\mathrm{ng}}^{\mathrm{SEPD,3D}} \approx \frac{1}{2}(x_{im} - x_{ir})\,\varphi_m - \frac{1}{2}(y_{im} - y_{ir})\,\eta_m\,. \tag{20}$$

A constant lateral or vertical beam offset, therefore, generates primarily a first order TTL coupling, see Fig. 7.

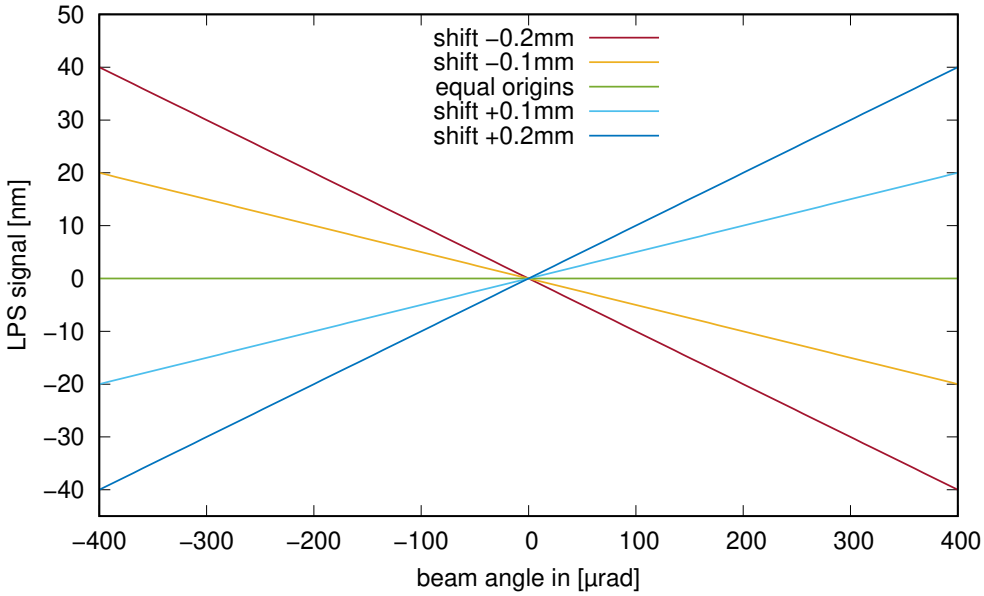

Figure 7. Simulated path length signal in the scenario with two identical Gaussian beams that only differ in their nominal points of incidence at the detector x_{im}. This describes a shift of the axis of the measurement beam by x_{im}, while having the centre of rotation at the same longitudinal distance from the beam's point of incidence. We find significant linear TTL coupling. The simulation parameters were: waist radius $w_0 = 1\,\text{mm}$, nominal points of incidence $x_{ir} = 0$ and $x_{im} = \{$-0.2 mm, -0.1 mm, 0 mm, 0.1 mm, 0.2 mm$\}$, centre of rotation at point of incidence, and detector radius 100 mm.

3.2.3. System jitter with arbitrary pivot and identical Gaussian beams Within this section, we consider the angular jitter of a receiving system. As we have shown in Sec. 2, the point of incidence of the measurement beam is not static in this case. Instead, the the offset of the point of rotation from the nominal point of incidence causes a beam walk on the detector surface, i.e. the measurement beam's incidence point shifts during the rotation: $(x_{im}, y_{im}) = (x_{im}(\varphi_m, \eta_m), y_{im}(\varphi_m, \eta_m))$. For small angles the beam walk can be linearised, such that cross-plane dependencies are being neglected, resulting in $(x_{im}(\varphi_m), y_{im}(\eta_m))$. Thereby, the centre of rotation considered in the derivation of the non-geometric TTL signal becomes angle-dependent.

In the particular case of an angularly jittering receiver, the pivot point is shifted longitudinally by d_{long}, laterally by d_{lat}, and vertically by d_{vert} with respect to the point of incidence (x_{im}, y_{im}).

In a two-dimensional case, the beam's horizontal offset x_{im} on the detector can be computed geometrically and we find

$$\begin{aligned} x^{\text{2D}}_{im,\text{RS}} = \; & x_{im,0} + \{d_{\text{long}} \sin(\varphi_{\text{RS}}) - d_{\text{lat}} \, [\sec(\varphi_{\text{RS}}) - 1]\} \\ & \cdot \cos(\varphi_{\text{RS}}) \sec(\varphi_{\text{RS}} - \varphi_{\text{PD}}) \qquad (21) \\ \approx \; & x_{im,0} + d_{\text{long}} \, \varphi_{\text{RS}} - \frac{1}{2} d_{\text{lat}} \, \varphi^2_{\text{RS}} \; , \qquad (22) \end{aligned}$$

where $x_{im,0}$ is the measurement beam's initial offset, i.e. its offset at $\varphi_{\text{RS}} = 0$. We can now substitute x_{im} in (18) by Eq. (22), using $\varphi_m \to -\varphi_{\text{RS}}$ and neglecting all additive

constants we find

$$\begin{aligned}\mathrm{LPS}_{\mathrm{ng,RS}}^{\mathrm{SEPD,2D}} \approx & -\frac{1}{2}(x_{im,0}-x_{ir})\varphi_{\mathrm{RS}} \\ & + \left[\frac{1}{2}\, d_{\mathrm{long}}\, \varphi_{\mathrm{RS}}\right] \left[-\varphi_{\mathrm{RS}} + \varphi_r - 2\varphi_{\mathrm{PD}}\right] . \end{aligned} \tag{23}$$

We find, that only the linear beam walk terms appear in the second-order expression (23). Extending our analysis to a three-dimensional case, we find for the linearised beam walk

$$x_{im,\mathrm{RS}}^{\mathrm{3D}} \approx x_{im,0} + d_{\mathrm{long}}\, \varphi_{\mathrm{RS}} \,, \tag{24}$$

$$y_{im,\mathrm{RS}}^{\mathrm{3D}} \approx y_{im,0} - d_{\mathrm{long}}\, \eta_{\mathrm{RS}} \,. \tag{25}$$

Inserting this into Eq. (19), we find the additional non-geometric TTL contribution originating from the arbitrary pivot location:

$$\begin{aligned}\mathrm{LPS}_{\mathrm{ng,RS}}^{\mathrm{SEPD,3D}} \approx & -\frac{1}{2}(x_{im,0}-x_{ir})\varphi_{\mathrm{RS}} + \frac{1}{2}(y_{im,0}-y_{ir})\eta_{\mathrm{RS}} \\ & - \frac{1}{2}\, d_{\mathrm{long}}\, \varphi_{\mathrm{RS}}(\varphi_{\mathrm{RS}} - \varphi_r) \\ & - \frac{1}{2}\, d_{\mathrm{long}}\, \eta_{\mathrm{RS}}(\eta_{\mathrm{RS}} - \eta_r) \,. \end{aligned} \tag{26}$$

Comparing Eq. (26) and Eq. (20) we see that a rotation around a pivot that is shifted longitudinally by d_{long} against the incidence point (x_{im}, y_{im}) of the measurement beam on the detector, results in additional first- and second-order non-geometric TTL coupling. Lateral displacement of the centre of rotation affects the beam walk only as a secondary effect (Eq. (22)). We neglected it in all further equations as higher than second-order effect due to x_{im} being multiplied to small angles in the computation of the non-geometric coupling via Eqs. (18) and (19). Therefore, the lateral displacement d_{lat} of the centre of rotation with respect to the nominal beam axis does not affect the non-geometric TTL coupling for small angles.

Lateral jitter coupling So far, we have only investigated the angular jitter of the receiver. We now consider the case of a laterally jittering spacecraft which is assumed to be angularly misaligned with respect to the incoming beam.

We define the lateral jitter of a receiver as the jitter along the y- or z-axis of the receiver, see Fig. 2. Due to this jitter, the measurement beam would get shifted along the detector surface and, therefore, the offset x_{im} of the point of detection of the measurement beam with respect to the detector centre becomes time-dependent. We describe the corresponding TTL coupling by substituting $\varphi_m \to -\varphi_{\mathrm{RS}}$ in Eq. (18) and by neglecting all terms that are constant in the case of lateral jitter coupling:

$$\mathrm{LPS}_{\mathrm{ng,RS}}^{\mathrm{SEPD,2D}} \approx \frac{1}{2}\, x_{im}(t) \left[-(\varphi_{\mathrm{RS}} + \varphi_{\mathrm{PD}}) + (\varphi_r - \varphi_{\mathrm{PD}})\right] . \tag{27}$$

Assuming an untilted detector, the variation of the incidence point $x_{im}(t)$ on the detector would directly correspond to the lateral jitter $y_{\mathrm{RS}}(t)$ of the receiving system, i.e.

$$\mathrm{LPS}_{\mathrm{ng,RS}}^{\mathrm{SEPD,2D}} \approx \frac{1}{2}\, y_{\mathrm{RS}}(t) \left(-\varphi_{\mathrm{RS}} + \varphi_r\right) . \tag{28}$$

If, on the other hand, the detector is tilted with respect to the internal receiver coordinate system, the beam walk corresponds to the jitter via

$$x_{im} \approx x_{im,0} + y_{\mathrm{RS}}(t)\left[1 + \frac{1}{2}\left(2\varphi_{\mathrm{RS}}\,\varphi_{\mathrm{PD}} + \varphi_{\mathrm{PD}}^2\right)\right] . \tag{29}$$

However, we have seen previously that second-order changes of the beam walk do only couple as higher-order terms into the non-geometric signal. Therefore, we find

$$\mathrm{LPS}_{\mathrm{ng,RS}}^{\mathrm{SEPD,2D}} \approx \frac{1}{2}\,y_{\mathrm{RS}}(t)\left[-(\varphi_{\mathrm{RS}} + \varphi_{\mathrm{PD}}) + (\varphi_r - \varphi_{\mathrm{PD}})\right] . \tag{30}$$

Eqs. (28) and (30) yield strong linear TTL coupling depending on the alignment of the interfering beams with respect to the detector surface.

LPS signal as sum of geometric and non-geometric effects We now use the equations above to reanalyse a setup previously described in [1, cf Fig. 9]. There, a system rotation with an arbitrary longitudinal offset of the pivot point, but no lateral offset was assumed. Both beams were in the nominal case aligned to each other, i.e. $x_{im,0} = x_{ir}$ and $\varphi_r = 0$, and we assumed no photodiode tilt, i.e. $\varphi_{\mathrm{PD}} = 0$. Inserting this into Eq. (18), we get

$$\mathrm{LPS}_{\mathrm{ng,RS}}^{\mathrm{SEPD,2D}} \approx -\frac{1}{2} d_{\mathrm{long}} \varphi_{\mathrm{RS}}^2 . \tag{31}$$

By comparing Eq. (31) with the corresponding OPD [1, cf Eq. (43)], we find that both are equal for a rotation of the system around a longitudinally displaced pivot but have an inverted sign. Thus, the angular jitter coupling for a longitudinally displaced centre of rotation cancels:

$$\begin{aligned} \mathrm{LPS}_{\mathrm{RS}}^{\mathrm{SEPD,2D}} &= \mathrm{OPD}_{\mathrm{RS}}^{\mathrm{2D}} + \mathrm{LPS}_{\mathrm{ng,RS}}^{\mathrm{SEPD,2D}} && (32)\\ &\approx 0 . && (33) \end{aligned}$$

This confirms the observations found in numerical simulations [1, 10]. Considering instead a laterally jittering receiving system with a constant angular misalignment ($\varphi_{\mathrm{RS}} \neq 0$), we find residual TTL coupling in the complete LPS signal. Let us, for simplicity, assume a nominally aligned reference beam and detector, i.e. $\varphi_r = \varphi_{\mathrm{PD}} = 0$, and no beam offsets on the detector, i.e. $x_{im,0} = x_{ir} = 0$. Under these assumptions, Eq. (28) reduces to

$$\mathrm{LPS}_{\mathrm{ng,RS}}^{\mathrm{SEPD,2D}} \approx -\frac{1}{2}\,y_{\mathrm{RS}}\,\varphi_{\mathrm{RS}} . \tag{34}$$

While seeing a significant non-geometric coupling for lateral jitter, there is no geometric correspondence: If the receiver jitters parallelly to its detector surface, the length of the received beam does not change [1, cf Eq. (38)]. Thus, the lateral TTL coupling here is fully described by the non-geometric coupling,

$$\mathrm{LPS}_{\mathrm{RS}}^{\mathrm{SEPD,2D}} = \mathrm{LPS}_{\mathrm{ng,RS}}^{\mathrm{SEPD,2D}} \approx -\frac{1}{2}\,y_{\mathrm{RS}}\,\varphi_{\mathrm{RS}} , \tag{35}$$

which yields a strong linear coupling.

3.2.4. Reflecting mirror with arbitrary pivot and identical Gaussian beams We now consider again the case of a mirror with angular jitter as depicted in Fig. 1 and an arbitrary pivot location. The offset x_{im} then depends on the mirror angle φ, the lever arm d_{lever} as well as the longitudinal and lateral displacements between the reflection point and the centre of rotation $d_{\text{long}}, d_{\text{lat}}$:

$$\begin{aligned} x_{im,\text{MR}}^{\text{2D}} \approx\ & x_{im,0} - \ 2\left[d_{\text{lever}} + d_{\text{lat}}\sin(\beta)\right]\varphi \\ & + \ \left[2d_{\text{lat}}\cos(\beta) + d_{\text{long}}\sin(\beta)\right]\varphi^2 . \end{aligned} \tag{36}$$

We can now substitute in Eq. (18) $\varphi_m \to 2\varphi$ and x_{im} by Eq. (36) and find

$$\begin{aligned} \text{LPS}_{\text{ng,MR}}^{\text{SEPD,2D}} \approx\ & (x_{im,0} - x_{ir})\,\varphi \\ & - \left[d_{\text{lever}} + d_{\text{lat}}\sin(\beta)\right]\varphi\,(2\varphi + \varphi_r - 2\varphi_{\text{PD}}) . \end{aligned} \tag{37}$$

We also expand this case for three-dimensional setups. For simplicity we assume a measurement beam with normal incidence ($\beta_y, \beta_z = 0$) on the test mass and no detector tilt. Then, the linearised tilt-dependent beam walk becomes

$$x_{im,\text{MR}}^{\text{3D}} \approx x_{im,0} - 2d_{\text{lever}}\varphi\,, \tag{38}$$

$$y_{im,\text{MR}}^{\text{3D}} \approx y_{im,0} + 2d_{\text{lever}}\eta\,. \tag{39}$$

We can use again Eq. (19) with $\varphi_m \to 2\varphi$ and $\eta_m \to 2\eta$, substitute x_{im}, y_{im} by Eq. (39) and find

$$\begin{aligned} \text{LPS}_{\text{ng,MR}}^{\text{SEPD,3D}} \approx\ & (x_{im,0} - x_{ir})\,\varphi - (y_{im,0} - y_{ir})\,\eta \\ & - d_{\text{lever}}\left(2\varphi^2 + \varphi\,\varphi_r + 2\eta^2 + \eta\,\eta_r\right) \end{aligned} \tag{40}$$

Both Eqs. (37) and (40) show that the non-geometric TTL coupling has first- and second-order contributions. Like in the case of a jittering receiver, an initial shift between the two beams causes linear non-geometric TTL coupling (first line in both equations). For any given lever arm or a lateral offset d_{lat}, an additional linear effect originates from an angular misalignment of the reference beam or a photodiode tilt. If both are optimally aligned, the beam walk would only yield second-order non-geometric TTL coupling.

LPS signal as sum of geometric and non-geometric effects Now, we can combine the non-geometric and the geometric TTL contributions to see the total effect and do this here for simplicity only for the two-dimensional case. Investigating the case of ideal alignment, i.e. $x_{im,0} = x_{ir}$, $\varphi_r = 0$, and using Eq. (10) from [1], we find a total LPS of

$$\text{LPS}_{\text{MR}}^{\text{SEPD,2D}} = \ \text{OPD}_{\text{MR}}^{\text{2D}} + \text{LPS}_{\text{ng,MR}}^{\text{SEPD,2D}} \tag{41}$$

$$\approx -2d_{\text{lat}}\cos(\beta)\varphi + d_{\text{long}}\cos(\beta)\varphi^2 . \tag{42}$$

Like in the previous section, we can show for the given case that the geometric and non-geometric lever arm effects cancel in the total TTL equations. However, the non-geometric piston effect does not fully cancel its geometric counterpart leaving the residual given in Eq. (42). The same holds for the more general case of arbitrarily aligned beams, only that more TTL coupling terms would appear in the residual. In conclusion,

we see that in a setup where neither the geometric nor the non-geometric TTL effects get suppressed, the total piston effect will be the dominant noise source since the total lever arm effect is zero. A lateral displacement d_{lat} of the centre of rotation relative to the incidence point on the detector causes linear coupling and should be avoided if possible. Contrary, a longitudinal displacement of the centre of rotation adds only second-order coupling and is, therefore, less critical.

Lateral jitter coupling The equations (36)-(42) hold for angular jitter coupling assuming time-dependent rotations $\varphi(t)$ and $\eta(t)$ as well as for lateral jitter coupling assuming a time-dependency of $d_{\mathrm{lat}}(t)$. Like before, we see in Eq. (40) that lateral jitter does not couple into the non-geometric LPS signal if the beams have a normal incidence on the mirror, i.e. $\beta_y, \beta_z = 0$. Contrary, Eq. (37) shows that lateral behaviour enters the signal if $\beta \neq 0$. However, this coupling is small for small lateral jitter since we multiply with quadratic angular misalignments giving in total a third-order effect. On the other hand, we see in Eq. (42) for the full signal that uncancelled geometric lateral jitter coupling induces significant TTL coupling.

3.2.5. Identical Gaussian beams with transmissive components along the measurement beam path The effect of transmissive components on the measurement beam path has previously been discussed in [1]. The beam refraction occurring due to the different refractive indices of the surrounding medium and the component's material changes the beam path within the component. Consequently, the beam is shifted laterally with respect to the path the beam would propagate if the transmissive component was not there. The respective beam walk is

$$x_{im,\mathrm{tc}}^{\mathrm{2D}} \approx -\sum_i t_{\mathrm{BS},i} \left[\frac{n_{\mathrm{BS},i}^2 \cos(\varphi_{\mathrm{BS},i})^2}{(n_{\mathrm{BS},i}^2 - \sin^2(\varphi_{\mathrm{BS},i}))^{3/2}} - \frac{\sin^2(\varphi_{\mathrm{BS},i})}{\sqrt{n_{\mathrm{BS},i}^2 - \sin^2(\varphi_{\mathrm{BS},i})}} - \cos(\varphi_{\mathrm{BS},i}) \right] \varphi_m$$
$$- \sum_i \frac{3}{2} \frac{n_{\mathrm{BS},i}^2 t_{\mathrm{BS},i} \cos(\varphi_{\mathrm{BS},i}) \sin(\varphi_{\mathrm{BS},i})}{((n_{\mathrm{BS},i}^2 - \sin^2(\varphi_{\mathrm{BS},i}))^{5/2}} \left(n_{\mathrm{BS},i}^2 - 1\right) \varphi_m^2 \,. \tag{43}$$

This equation can be used both for the case of angular jitter of a system (replace $\varphi_m \to -\varphi_{\mathrm{RS}}$) or of a mirror ($\varphi_m \to 2\varphi$). The total beam walk is then the sum of Eq. (43) and the offsets derived for a rotation of the setup (Eq. (22)) or the mirror (Eq. (36)):

$$x_{im,\mathrm{MRT}} = x_{im,\mathrm{MR}} + x_{im,\mathrm{tc}} \,, \tag{44}$$
$$x_{im,\mathrm{RST}} = x_{im,\mathrm{RS}} + x_{im,\mathrm{tc}} \,. \tag{45}$$

In the given case of identical beam parameters, this sum of beam walks results also in a full non-geometric LPS signal which is a sum of the previously derived terms, and an additional LPS signal due to the transmissive component:

$$\mathrm{LPS}_{\mathrm{ng,MRT}} = \mathrm{LPS}_{\mathrm{ng,MR}} + \mathrm{LPS}_{\mathrm{ng,tc}}^{\mathrm{SEPD}} \,, \tag{46}$$
$$\mathrm{LPS}_{\mathrm{ng,RST}} = \mathrm{LPS}_{\mathrm{ng,RS}} + \mathrm{LPS}_{\mathrm{ng,tc}}^{\mathrm{SEPD}} \,. \tag{47}$$

In the two-dimensional case, the additive term reads

$$\mathrm{LPS}_{\mathrm{ng,tc}}^{\mathrm{SEPD,2D}} \approx -\sum_i \frac{t_{\mathrm{BS},i}}{2}\left[\frac{n_{\mathrm{BS},i}^2\cos(\varphi_{\mathrm{BS},i})^2}{(n_{\mathrm{BS},i}^2-\sin^2(\varphi_{\mathrm{BS},i}))^{3/2}} - \frac{\sin^2(\varphi_{\mathrm{BS},i})}{\sqrt{n_{\mathrm{BS},i}^2-\sin^2(\varphi_{\mathrm{BS},i})}} - \cos(\varphi_{\mathrm{BS},i})\right]\varphi_m\left[\varphi_m+\varphi_r-2\varphi_{\mathrm{PD}}\right]. \tag{48}$$

LPS signal as sum of geometric and non-geometric effects Transmissive components equally affect the geometric TTL coupling [1, cf Eq. (26)]. It can then be shown that the transmissive component dependent geometric and non-geometric TTL terms cancel in the full TTL signal

$$\mathrm{LPS}_{\mathrm{tc}}^{\mathrm{SEPD,2D}} = \mathrm{OPD}_{\mathrm{tc}}^{\mathrm{2D}} + \mathrm{LPS}_{\mathrm{ng,tc}}^{\mathrm{SEPD,2D}} \tag{49}$$

$$\approx 0\,. \tag{50}$$

provided that the reference beam is nominally aligned, i.e. $\varphi_r = 0$.

In summary, transmissive components do not contribute to angular or lateral jitter TTL coupling if both beams feature the same beam parameters and the reference beam impinges with a normal incidence at the detector.

3.2.6. Arbitrary Gaussian beams with arbitrary centre of rotation In the previous examples, the measurement and reference beam had initially the same intensity and phase profile on the detector. However, this is not representative for interferometers like LISA, GRACE-FO, or arbitrary instruments that use heterodyne interferometers where identical beam parameters are effectively not achievable. A beam parameter mismatch has a strong influence on the cross-coupling. The main reason for this is a discrepancy between the wavefront curvatures and diameter of the beams in the detector plane. A qualitative analysis of this effect can be found in [22].
Here, we provide an analytic expression for the non-geometric part of the path length measurement as we have done for the previous simpler cases. We find

$$\begin{aligned}\mathrm{LPS}_{\mathrm{ng}}^{\mathrm{SEPD,2D}} = (x_{im}-x_{ir})&\left[\frac{z_{Rm}(z_{Rm}+z_{Rr})+z_m(z_m-z_r)}{(z_{Rm}+z_{Rr})^2+(z_m-z_r)^2}(\varphi_m-\varphi_{\mathrm{PD}})\right.\\ &\left.+\frac{z_{Rr}(z_{Rm}+z_{Rr})-z_r(z_m-z_r)}{(z_{Rm}+z_{Rr})^2+(z_m-z_r)^2}(\varphi_r-\varphi_{\mathrm{PD}})\right]\\ -&\left\{\frac{z_{Rr}z_m+z_{Rm}z_r}{k((z_{Rm}+z_{Rr})^2+(z_m-z_r)^2)}\right.\\ &\left.+\frac{(x_{im}-x_{ir})^2}{(z_{Rm}+z_{Rr})^2+(z_m-z_r)^2}\left[z_m-\frac{2(z_{Rm}+z_{Rr})(z_{Rr}z_m+z_{Rm}z_r)}{(z_{Rm}+z_{Rr})^2+(z_m-z_r)^2}\right]\right\}\\ &\cdot\left(\frac{\varphi_m^2}{2}-\varphi_m\varphi_{\mathrm{PD}}\right)\\ -&\left[\frac{(z_{Rr}^2+z_r^2)z_m-(z_{Rm}^2+z_m^2)z_r}{(z_{Rm}+z_{Rr})^2+(z_m-z_r)^2}\right]\left(\frac{\varphi_m^2}{2}-\varphi_m\varphi_r\right)\end{aligned}$$

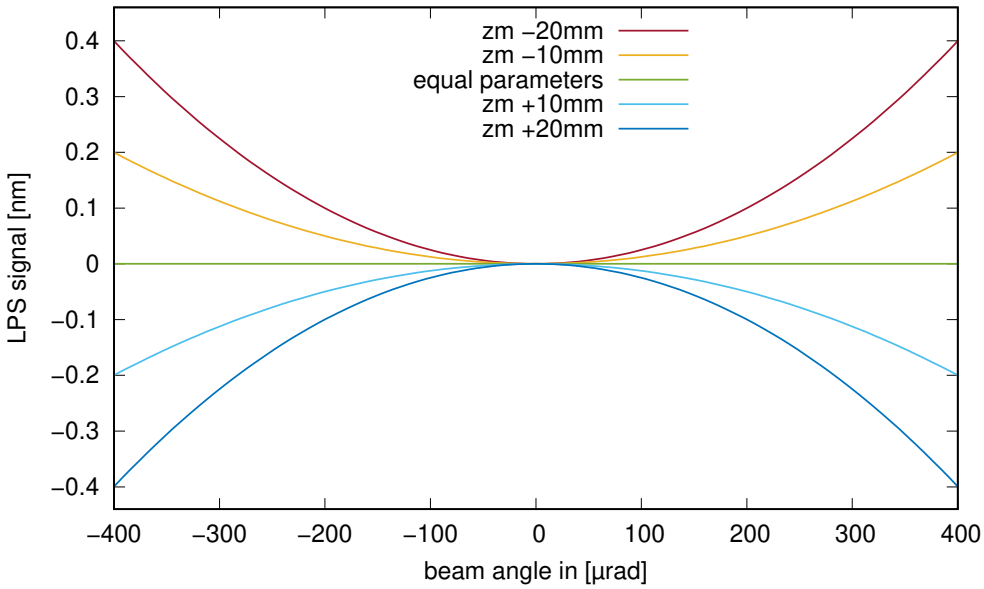

Figure 8. Simulated path length signal in the scenario with two Gaussian beams that only differ in their waist location and interfere on an infinitely large detector. All graphs go through the origin because we chose for each setting the signal obtained at a beam angle of zero as a reference and subtracted it from each curve. We find quadratic TTL coupling for this case of varying the waist location. The simulation parameters were: waist radius of both beams $w_0 = 1\,\mathrm{mm}$, nominal distances from waist at detector $z_r = 100\,\mathrm{mm}$ and $z_m = z_r + \{$-20 mm, -10 mm, 0 mm, 10 mm, 20 mm$\}$, pivot position at point of incidence, and detector radius 100 mm.

$$+ (x_{im} - x_{ir})^2 \left[\frac{(z_m - z_r)}{2\left((z_{Rm} + z_{Rr})^2 + (z_m - z_r)^2\right)}\right], \tag{51}$$

where x_{im} can be either static or dynamic as introduced in the previous subsection. Similar to the case of equal beam parameters, we can neglect some terms in Eq. (51) since they are negligible in common interferometric setups. We neglected the terms featuring a division by the wavenumber k, or a product of a squared beam offset on the detector and a quadric tilt dependency, and find

$$\begin{aligned}\mathrm{LPS}_{\mathrm{ng}}^{\mathrm{SEPD,2D}} \approx (x_{im} - x_{ir})\Bigg[&\frac{z_{Rm}(z_{Rm} + z_{Rr}) + z_m(z_m - z_r)}{(z_{Rm} + z_{Rr})^2 + (z_m - z_r)^2}(\varphi_m - \varphi_{\mathrm{PD}}) \\ &+ \frac{z_{Rr}(z_{Rm} + z_{Rr}) - z_r(z_m - z_r)}{(z_{Rm} + z_{Rr})^2 + (z_m - z_r)^2}(\varphi_r - \varphi_{\mathrm{PD}})\Bigg] \\ &- \left[\frac{(z_{Rr}^2 + z_r^2)z_m - (z_{Rm}^2 + z_m^2)z_r}{(z_{Rm} + z_{Rr})^2 + (z_m - z_r)^2}\right]\left(\frac{\varphi_m^2}{2} - \varphi_m\varphi_r\right) \\ &+ (x_{im} - x_{ir})^2 \left[\frac{(z_m - z_r)}{2\left((z_{Rm} + z_{Rr})^2 + (z_m - z_r)^2\right)}\right].\end{aligned} \tag{52}$$

By setting $z_{Rm} = z_{Rr}$ and $z_m = z_r$, Eq. (52) reduces to the case of equal beam parameters (compare Eq. (18)).

Though Eq. (52) is a fairly complex equation, it gives valuable information, for instance, if only single parameter changes are investigated at a time. Changing, for

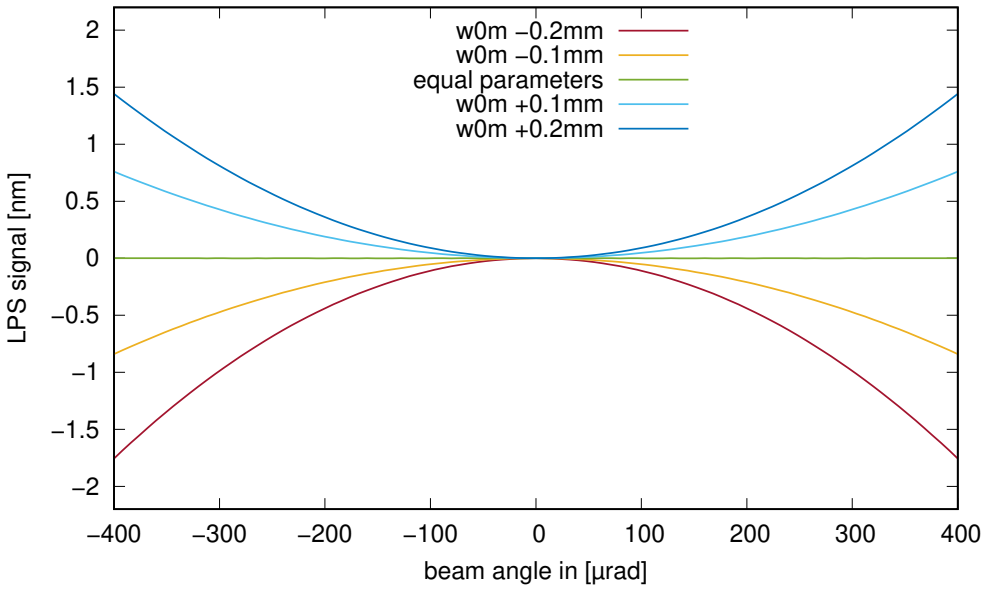

Figure 9. Simulated path length signal in the scenario with two Gaussian beams that only differ in their waist size and interfere on an infinitely large detector. All graphs go through the origin because we chose for each setting the signal obtained at a beam angle of zero as reference and subtracted it from each curve. We find quadratic TTL coupling for this case of varying the waist sizes. The simulation parameters were: waist radii $w_{0r} = 1\,\mathrm{mm}$ and $w_{0m} = w_{0r} + \{$-0.2 mm, -0.1 mm, 0 mm, 0.1 mm, 0.2 mm$\}$, nominal distances from waist at detector $z_m = z_r = 100\,\mathrm{mm}$, $x_{im} = x_{ir}$, pivot position at point of incidence, and detector radius 100 mm.

example, the distance from waist of the measurement beam with respect to the reference beam gives a quadratic TTL coupling as shown in Fig. 8. Changing the waist sizes of the beam instead, while keeping the other parameters identical, will likewise generate second-order TTL coupling, see Fig. 9. This shows that the TTL coupling is a mixture of linear and second-order terms for arbitrary beam parameter mismatches.

Arbitrary centre of rotation Compared to Eq. (18), the effect of beam walk on the non-geometric TTL coupling is different for unequal beam parameters. Therefore, we now evaluate the beam parameter-dependent TTL coupling also for arbitrary centres of rotation. For this, we substitute again x_{im} by its dynamic representation and assume for simplicity a nominally impinging reference beam ($\varphi_r = 0$) and no detector tilt ($\varphi_{\mathrm{PD}} = 0$). In the case of a rotation of the receiving system, we therefore substitute x_{im} by Eq. (22) in Eq. (52) and replace $\varphi_m \to -\varphi_{\mathrm{RS}}$ giving

$$\begin{aligned}\mathrm{LPS}_{\mathrm{ng,RS}}^{\mathrm{SEPD,2D}} \approx &-(x_{im,0} - x_{ir})\frac{z_{Rm}(z_{Rm}+z_{Rr}) + z_m(z_m - z_r)}{(z_{Rm}+z_{Rr})^2 + (z_m - z_r)^2}\,\varphi_{\mathrm{RS}} \\ &+ d_{\mathrm{long}}\,(x_{im,0} - x_{ir})\left[\frac{(z_m - z_r)}{(z_{Rm}+z_{Rr})^2 + (z_m - z_r)^2}\right]\varphi_{\mathrm{RS}} \\ &- d_{\mathrm{long}}\left[\frac{z_{Rm}(z_{Rm}+z_{Rr}) + z_m(z_m - z_r)}{(z_{Rm}+z_{Rr})^2 + (z_m - z_r)^2}\right]\varphi_{\mathrm{RS}}^2\end{aligned}$$

$$+ \left(d_{\text{long}}^2 - d_{\text{lat}}\left(x_{im,0} - x_{ir}\right)\right) \left[\frac{(z_m - z_r)}{2\left((z_{Rm} + z_{Rr})^2 + (z_m - z_r)^2\right)}\right] \varphi_{\text{RS}}^2$$
$$- \left[\frac{(z_{Rr}^2 + z_r^2)z_m - (z_{Rm}^2 + z_m^2)z_r}{(z_{Rm} + z_{Rr})^2 + (z_m - z_r)^2}\right] \frac{\varphi_{\text{RS}}^2}{2}\,. \tag{53}$$

Analogously we proceed for the mirror rotation, where we substitute x_{im} by Eq. (36) and $\varphi_m \to 2\varphi$. Thus we find

$$\begin{aligned}
&\text{LPS}_{\text{ng,MR}}^{\text{SEPD,2D}} \\
&\approx\ 2(x_{im,0} - x_{ir})\frac{z_{Rm}(z_{Rm} + z_{Rr}) + z_m(z_m - z_r)}{(z_{Rm} + z_{Rr})^2 + (z_m - z_r)^2}\,\varphi \\
&-\ 2\left[d_{\text{lever}} + d_{\text{lat}}\sin(\beta)\right]\ \left(x_{im,0} - x_{ir}\right)\ \left[\frac{(z_m - z_r)}{(z_{Rm} + z_{Rr})^2 + (z_m - z_r)^2}\right]\varphi \\
&-\ 4\left[d_{\text{lever}} + d_{\text{lat}}\sin(\beta)\right]\left[\frac{z_{Rm}(z_{Rm} + z_{Rr}) + z_m(z_m - z_r)}{(z_{Rm} + z_{Rr})^2 + (z_m - z_r)^2}\right]\varphi^2 \\
&+\ \left\{2\left[d_{\text{lever}} + d_{\text{lat}}\sin(\beta)\right]^2 + \left[2d_{\text{lat}}\cos(\beta) + d_{\text{long}}\sin(\beta)\right]\ \left(x_{im,0} - x_{ir}\right)\right\} \\
&\quad \cdot \left[\frac{(z_m - z_r)}{(z_{Rm} + z_{Rr})^2 + (z_m - z_r)^2}\right]\varphi^2 \\
&-\ 2\left[\frac{(z_{Rr}^2 + z_r^2)z_m - (z_{Rm}^2 + z_m^2)z_r}{(z_{Rm} + z_{Rr})^2 + (z_m - z_r)^2}\right]\varphi^2\,.
\end{aligned} \tag{54}$$

Last, we investigate this case for beams passing through transmissive components. By substituting the beam walk by Eq. (43), we find

$$\begin{aligned}
&\text{LPS}_{\text{ng,tc}}^{\text{SEPD,2D}} \\
&\approx\ (x_{im,0} - x_{ir})\frac{z_{Rm}(z_{Rm} + z_{Rr}) + z_m(z_m - z_r)}{(z_{Rm} + z_{Rr})^2 + (z_m - z_r)^2}\varphi_m \\
&-\ \sum_i t_{\text{BS},i}\left[\frac{n_{\text{BS},i}^2\cos(\varphi_{\text{BS},i})^2}{(n_{\text{BS},i}^2 - \sin^2(\varphi_{\text{BS},i}))^{3/2}} - \frac{\sin^2(\varphi_{\text{BS},i})}{\sqrt{n_{\text{BS},i}^2 - \sin^2(\varphi_{\text{BS},i})}} - \cos(\varphi_{\text{BS},i})\right] \\
&\qquad \cdot \left(x_{im,0} - x_{ir}\right)\ \left[\frac{(z_m - z_r)}{(z_{Rm} + z_{Rr})^2 + (z_m - z_r)^2}\right]\varphi_m \\
&-\ \sum_i t_{\text{BS},i}\left[\frac{n_{\text{BS},i}^2\cos(\varphi_{\text{BS},i})^2}{(n_{\text{BS},i}^2 - \sin^2(\varphi_{\text{BS},i}))^{3/2}} - \frac{\sin^2(\varphi_{\text{BS},i})}{\sqrt{n_{\text{BS},i}^2 - \sin^2(\varphi_{\text{BS},i})}} - \cos(\varphi_{\text{BS},i})\right] \\
&\qquad \cdot \left[\frac{z_{Rm}(z_{Rm} + z_{Rr}) + z_m(z_m - z_r)}{(z_{Rm} + z_{Rr})^2 + (z_m - z_r)^2}\right]\varphi_m^2 \\
&+\ \left\{\left(\sum_i t_{\text{BS},i}\left[\frac{n_{\text{BS},i}^2\cos(\varphi_{\text{BS},i})^2}{(n_{\text{BS},i}^2 - \sin^2(\varphi_{\text{BS},i}))^{3/2}} - \frac{\sin^2(\varphi_{\text{BS},i})}{\sqrt{n_{\text{BS},i}^2 - \sin^2(\varphi_{\text{BS},i})}} - \cos(\varphi_{\text{BS},i})\right]\right)^2\right. \\
&\qquad \left. - \sum_i \frac{3}{2}\,\frac{n_{\text{BS},i}^2 t_{\text{BS},i}\cos(\varphi_{\text{BS},i})\sin(\varphi_{\text{BS},i})}{((n_{\text{BS},i}^2 - \sin^2(\varphi_{\text{BS},i}))^{5/2}}\left(n_{\text{BS},i}^2 - 1\right)\ \left(x_{im,0} - x_{ir}\right)\right\} \\
&\qquad \cdot \left[\frac{(z_m - z_r)}{(z_{Rm} + z_{Rr})^2 + (z_m - z_r)^2}\right]\varphi_m^2
\end{aligned}$$

$$- \left[\frac{(z_{Rr}^2 + z_r^2)z_m - (z_{Rm}^2 + z_m^2)z_r}{(z_{Rm} + z_{Rr})^2 + (z_m - z_r)^2}\right] \frac{\varphi_m^2}{2} \,. \tag{55}$$

In all three cases, we find analogously to the cases with equal beam parameters (Eqs. (23), (37) and (48)) that the linear terms disappear, if the two beams are nominally aligned, i.e. $x_{im,0} = x_{ir}$. In general, the dynamic beam walk adds first- and second-order TTL coupling.

We see that dynamic beam walk couples with the non-equal beam parameters. Hence these terms cannot (partially) cancel with the geometric TTL coupling as in the case of equal beam parameters (compare Eqs. (33), (42) and (50)).

However, we can construct a special case where it does indeed cancel. The waist size becomes irrelevant when considering a rotation around the waist position. Let both beams be identical besides their waist size and imping nominally at the non-tilted detector, i.e. $z_m = z_r$, $x_{im,0} = x_{ir}$, $\varphi_r = 0$ and $\varphi_{\mathrm{PD}} = 0$. The centre of rotation is longitudinally displaced from the detector surface and lies in the beam waist, i.e. $d_{\mathrm{long}} = z_m$. In this case, the geometric and the non-geometric TTL effects cancel each other.

$$\begin{aligned}
\mathrm{LPS}_{\mathrm{RS}}^{\mathrm{SEPD,2D}} &= \mathrm{OPD}_{\mathrm{RS}}^{\mathrm{2D}} + \mathrm{LPS}_{\mathrm{ng,RS}}^{\mathrm{SEPD,2D}} && (56)\\
&\approx \left[d_{\mathrm{long}} \frac{\varphi_{\mathrm{RS}}^2}{2}\right] - \left[d_{\mathrm{long}}\, \varphi_{\mathrm{RS}}\right] \left[\frac{z_{Rm}}{z_{Rm} + z_{Rr}}\right] \varphi_{\mathrm{RS}} \\
&\quad - \left[\frac{(z_{Rr} - z_{Rm})\, d_{\mathrm{long}}}{z_{Rm} + z_{Rr}}\right] \frac{\varphi_{\mathrm{RS}}^2}{2} && (57)\\
&= 0 \,. && (58)
\end{aligned}$$

3.2.7. Wavefront errors We have so far generally assumed the idealised case of perfect fundamental Gaussian beams with axial symmetry. In experimental reality, the interfering Gaussian wavefronts will have small distortions that can, for instance, be described by a superposition of higher-order modes with low amplitudes. These superimposing modes then affect the symmetry of the Gaussian beams, as illustrated in Fig. 10. Consequently, wavefront errors affect the TTL coupling behaviour. These additional wavefront error dependent TTL effects cannot be easily modelled for all the discussed cases. So instead, we assume a fairly arbitrary TTL contribution, which then in a Taylor series expansion up to second-order would be containing both first- and second-order contributions. Some numerical simulation programs can handle these wavefront errors and consider them in the final signal, e.g., IfoCAD [3, 20].

3.3. TTL effects originating from detector properties

Not only do the wavefront properties of the beams affect the LPS signal, but also the detector geometry itself contributes to the cross-coupling. Mathematically, this can be seen from the integral over the detector surface S in Eq. (4), which is used for computing an LPS signal using Eq. (5). We will therefore investigate below the various contributions to $\mathrm{LPS}_{\mathrm{ng}}$ originating from detector properties. In Sec. 3.3.1 we show that

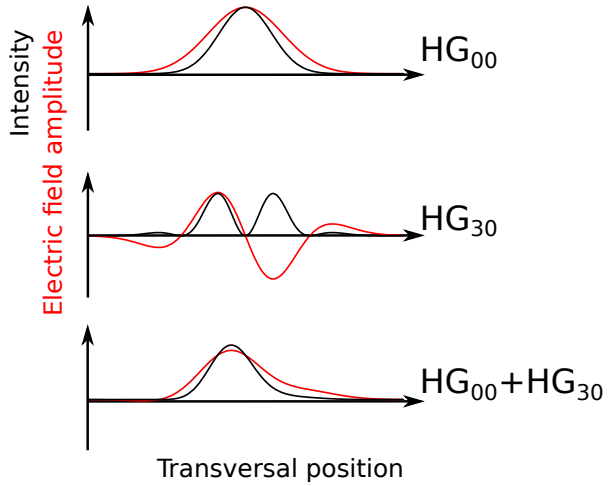

Figure 10. A fundamental mode is mixed with a HG_{30} mode, the resulting amplitude and intensity profiles of the resulting beam are asymmetric (previously shown in [22]).

the photodiode angle cancels from the LPS signal and can, therefore, be directly set to zero in simulations, independent of the corresponding experimental value. In Sec. 3.3.2 we then show that different definitions of the LPS signal exist if quadrant diodes are used. These different LPS signal types usually show different amounts of TTL coupling. We then show in Sec. 3.3.3 how phase contributions for finite square quadrant photodiodes can be computed analytically. Finally, we briefly discuss the effect of diode imperfections in Sec. 3.3.4.

3.3.1. Tilt of the detector The photodiode angle affects the geometric (see [1, cf Eqs. (30) and (31)]), as well as the non-geometric (see Sec. 3.2) contributions to the total TTL coupling. This is natural for the beam axes of the measurement and reference beam, which need to propagate a different optical path length dependent on the detector angle. However, this does not necessarily also hold for the interferometric phase. Since both beams are brought to interference on a beam recombiner prior to the photodiode, both beams experience the same phase changes from this point to the detector. A tilt of the detector surface is then a change that equally affects the reference and measurement beam, as well as their relative phase in each detector point. This is shown in Fig. 11. There, the TTL coupling for unequal beam parameters is compared for the case of an un-tilted photodiode (left part of the image), with the case of a tilted photodiode (right part of the image). Even though the complex amplitude vectors in each detector point slightly change due to the detector tilt, we could not find an effect on the total phase (green arrows). The detector angle is therefore expected to either cancel from the LPS signal or to be small, i.e. much smaller than we would expect from geometric TTL estimates.

To confirm this expectation, we focus on the photodiode angle dependent terms in the $\mathrm{LPS} = \mathrm{OPD} + \mathrm{LPS}_{\mathrm{ng}}$ and, therefore, subtract all terms not depending on φ_{PD}, i.e.

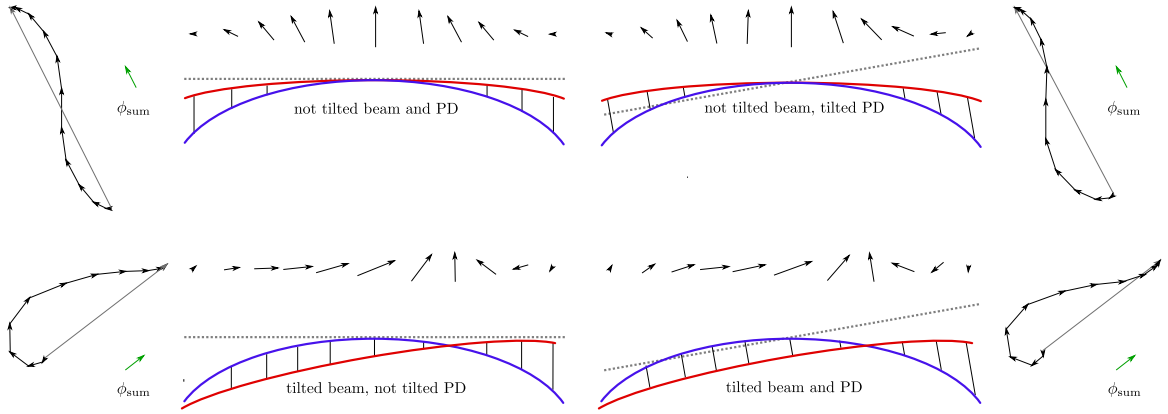

Figure 11. Qualitative analysis of the TTL coupling for unequal beam parameters showing that the photodiode angle does not contribute to the TTL coupling. The left-hand side shows the case of a non-tilted detector ($\varphi_{\mathrm{PD}} = 0$), the right-hand side the case of a tilted detector. Upper left figure: Neither the beams nor the detector is tilted. Lower left figure: Non-tilted detector, but the measurement beam (red) got tilted with respect to the reference beam (blue). The total phase changed in comparison to the non-tilted case, implying TTL coupling. Upper and lower right figures: same as the corresponding left figures, but the detector surface was tilted. This tilt changes the direction along which the complex amplitudes are being defined and read out (see connecting lines between the blue and red curves), such that all vector representations of the complex amplitudes are slightly changed. However, no change of the total phases can be observed here compared to the cases without detector tilt.

$\mathrm{LPS}(\varphi_{\mathrm{PD}} = 0)$, and find

$$\mathrm{LPS}^{\mathrm{SEPD,2D}}(\varphi_{\mathrm{PD}}) - \mathrm{LPS}^{\mathrm{SEPD,2D}}(\varphi_{\mathrm{PD}} = 0) \approx 0\,. \tag{59}$$

We see that all considerable first- and second-order detector tilt dependent TTL terms cancel out in the full LPS signal. This evaluation applies to the case of a mirror rotation substituting $\mathrm{OPD}^{\mathrm{2D}}_{\mathrm{MRT}}$ ([1, cf Eq. (30)]) for the geometric and $\mathrm{LPS}^{\mathrm{SEPD,2D}}_{\mathrm{ng}}$ (Eq. (52)) for the non-geometric contribution with $x^{\mathrm{2D}}_{im,\mathrm{MRT}}$ (Eq. (44)) as well for a rotation of the receiving system substituting $\mathrm{OPD}^{\mathrm{2D}}_{\mathrm{RST}}$ ([1, cf Eq. (31)]) and $\mathrm{LPS}^{\mathrm{SEPD,2D}}_{\mathrm{ng}}$ (Eq. (52)) with $x^{\mathrm{2D}}_{im,\mathrm{RST}}$ (Eq. (45)).

We conclude from this that in any derivation of LPS signals for large SEPDs, the photodiode angle φ_{PD} can be neglected even if the diode is in the corresponding experiment indeed tilted. Nonetheless, we show all equations with φ_{PD} here because ray tracing tools computing the OPD will always include this term. For better agreements between a simulated OPD and LPS and corresponding experimental results, it is, therefore, advisable to set $\varphi_{\mathrm{PD}} = 0$ in simulations.

3.3.2. Dependence on the path length signal definition using QPDs So far, we have assumed infinitely large SEPDs as detectors, which means that both wavefronts are fully sensed by the detector and no clipping occurs. This assumption is not valid in cases where a quadrant photodiode (QPD) is being used for angular sensing using differential

wavefront sensing (DWS) [23]. QPDs further allow for multiple phase signal definitions [24] which contribute differently to the overall cross-coupling. This originates from the fact that every photodiode quadrant delivers an individual photocurrent, and, therefore, an individual complex amplitude. Mathematically, this is described by evaluating the surface integral in Eq. (13) over the corresponding quadrant i, resulting in the complex amplitude a_i. The four complex amplitudes can then be combined in different ways to generate the total phase readout ϕ and the corresponding LPS signal. We show this here exemplary for two commonly used QPD path length definitions, the arithmetic mean phase and the LISA Pathfinder LPS signal.

The arithmetic mean phase (AP) is literally derived from the arithmetic mean of the phases of the four segments

$$\phi^{\mathrm{AP}} = \frac{\arg(a_{\mathrm{A}}) + \arg(a_{\mathrm{B}}) + \arg(a_{\mathrm{C}}) + \arg(a_{\mathrm{D}})}{4} \tag{60}$$

$$= \frac{\phi_{\mathrm{A}} + \phi_{\mathrm{B}} + \phi_{\mathrm{C}} + \phi_{\mathrm{D}}}{4}\,, \tag{61}$$

where A,B,C,D denote the four quadrants of the photodiode. The corresponding LPS signal is then defined like before (see Eq. (5)):

$$\mathrm{LPS}^{\mathrm{AP}} = \frac{\phi^{\mathrm{AP}}}{k} = \frac{\phi_{\mathrm{A}} + \phi_{\mathrm{B}} + \phi_{\mathrm{C}} + \phi_{\mathrm{D}}}{4k}\,. \tag{62}$$

This is a kind of a natural procedure when the signal is processed by a digital phase-locked loop (DPLL) based phasemeter that produces phases as primary output and not complex amplitudes [25].

The second signal definition we discuss here is called LISA Pathfinder (LPF) LPS signal definition because it was used in the LISA Pathfinder phasemeter, which uses an SBDFT. The result of which is a complex amplitude [26]. It is defined as the argument of the sum of all complex amplitudes, divided by k:

$$\mathrm{LPS}^{\mathrm{LPF}} = \frac{1}{k}\arg(a_{\mathrm{A}} + a_{\mathrm{B}} + a_{\mathrm{C}} + a_{\mathrm{D}})\,. \tag{63}$$

For a QPD with slits of zero width, the sum of the complex amplitudes of the single quadrants, corresponding to a sum of the integrals of the single segments, is equal to the complex amplitude of the entire diode. Therefore, for a slit diameter of zero the LISA Pathfinder QPD path length definition ($\mathrm{LPS}^{\mathrm{LPF}}$) becomes equal to the SEPD path length definition ($\mathrm{LPS}^{\mathrm{SEPD}}$) [24].

Figures 12 and 13 illustrate the effect of different wavefront curvatures on the cross-coupling if either the $\mathrm{LPS}^{\mathrm{LPF}}$ or $\mathrm{LPS}^{\mathrm{AP}}$ signal is used. In the centre, two interfering wavefronts are shown, with equal curvatures in Fig. 12, and with unequal curvatures in Fig. 13. Depending on the total phase signal definition, the complex amplitude vectors are recombined here in different ways. On the right, the LPF definition sums up all shown complex amplitude vectors of the left- and right-hand sides. On the left, the AP signal calculation is illustrated. Here, the complex amplitude vectors of the left and right-hand sides are added separately, resulting in a phase of the left- and right-hand sides (small grey arrows). These complex amplitude vectors are then added and

normalised again resulting in the green arrow which illustrates the averaged phase. In the case of equal wavefront curvatures, Fig. 12, the overall phase (i.e. the angle of the green arrow) is independent of the tilt angle for both phase definitions. That means that, like in the case of an SEPD, we do not expect TTL coupling for either of the LPS definitions if the interfering wavefronts have matched beam parameters.

Contrary, in the case of unequal wavefront curvatures in Fig. 13, the overall LPF phase changes if the wavefront tilts, while the overall AP phase is unaffected by tilts. Hence, in the case of unmatched wavefront properties and a rotation around the centre of the QPD, we expect that the AP signal shows less TTL coupling than the LPF signal. We confirm this using IfoCAD as shown in Fig. 14 for two aligned beams with identical parameters besides their waist size and a rotation of the measurement beam around their shared point of incidence. By Fig. 14, we demonstrate that the resulting AP signal comprises less TTL coupling than the LPF signal. Furthermore, the image shows that the LPF signal and the SEPD signal have nearly identical TTL coupling. This is expected from the definition of $\mathrm{LPS}^{\mathrm{LPF}}$. Finally, this demonstrates that using quadrant diodes and an AP signal can in some cases reduce the TTL coupling noise in the system. This was previously also observed in [27, 28].

3.3.3. TTL contributions comparing infinite SEPDs with finite square QPDs We show in this section that the TTL estimates for large SEPDs are still useful in cases, where small square SEPDs or QPDs and the LPF LPS signal are used. The derived signal contains the large SEPD's signal, though an additional TTL term originating from the clipping needs to be considered.

To account for phase changes due to clipping on the detector surface, we repeat the analytic derivation introduced in Sec. 3.1 but assume this time a square finite quadrant photodiode shape. This means, we integrate the complex product of the electrical fields over the detector surface, see Eq. (4) and compare [3, 21]. Transforming the electrical fields into photodiode coordinates x, y, we can rewrite Eq. (4) via

$$\phi = \arg\left[\int_{\mathrm{PD}} \mathrm{d}S \, \exp\left(C_{xx}x^2 + C_x x + C_{yy}y^2 + C_y y + C_0\right)\right] \tag{64}$$

where $C_i \in \mathbb{C}$. The integration over the detector surface gives

$$\begin{aligned}\phi = \arg\Bigg\{ & \frac{\pi \exp\left[\frac{1}{4}\left(\frac{C_x^2}{C_{xx}} + \frac{C_y^2}{C_{yy}} - 4C_0\right)\right]}{\sqrt{C_{xx}}\sqrt{C_{yy}}} \\ & \times \left[\frac{1}{4}\operatorname{erf}\left(\frac{C_x + C_{xx}\,x}{2\sqrt{C_{xx}}}\right)\right]\left[\frac{1}{4}\operatorname{erf}\Big(\frac{C_y + C_{yy}\,y}{2\sqrt{C_{yy}}}\Big)\right]\Big|_{\mathrm{PD}}\Bigg\} \end{aligned} \tag{65}$$

$$\begin{aligned} = \arg\Bigg\{ & \frac{\pi \exp\left[\frac{1}{4}\left(\frac{C_x^2}{C_{xx}} + \frac{C_y^2}{C_{yy}} - 4C_0\right)\right]}{\sqrt{C_{xx}}\sqrt{C_{yy}}}\Bigg\} \\ & + \arg\Big\{\Big[\frac{1}{4}\operatorname{erf}\Big(\frac{C_x + C_{xx}\,x}{2\sqrt{C_{xx}}}\Big)\Big]\Big[\frac{1}{4}\operatorname{erf}\Big(\frac{C_y + C_{yy}\,y}{2\sqrt{C_{yy}}}\Big)\Big]\Big|_{\mathrm{PD}}\Big\}, \end{aligned} \tag{66}$$

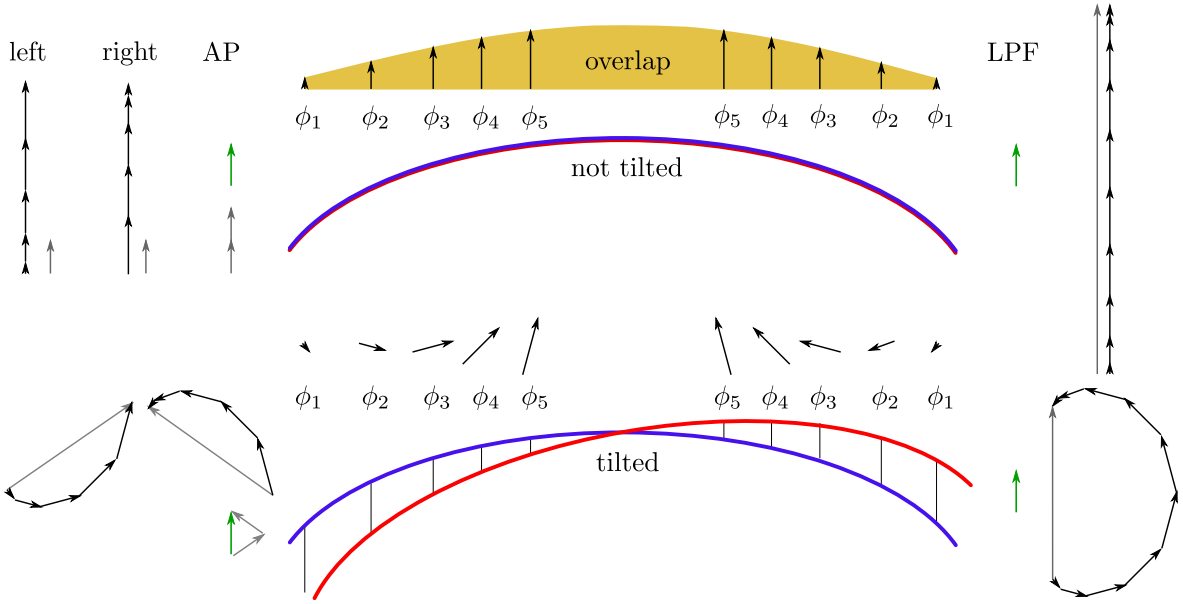

Figure 12. The effect of different path length definitions on the overall phase in the case of equal wavefront curvatures. On the right, the LPF definition sums up all complex amplitude vectors. On the left, the AP definition, i.e. Eq. (62), is used for two segments, which computes an average phase per side (left and right) and adds the averaged side complex amplitude vectors (grey arrows). The overall phase (green arrow) is independent of the tilt angle for both phase definitions.

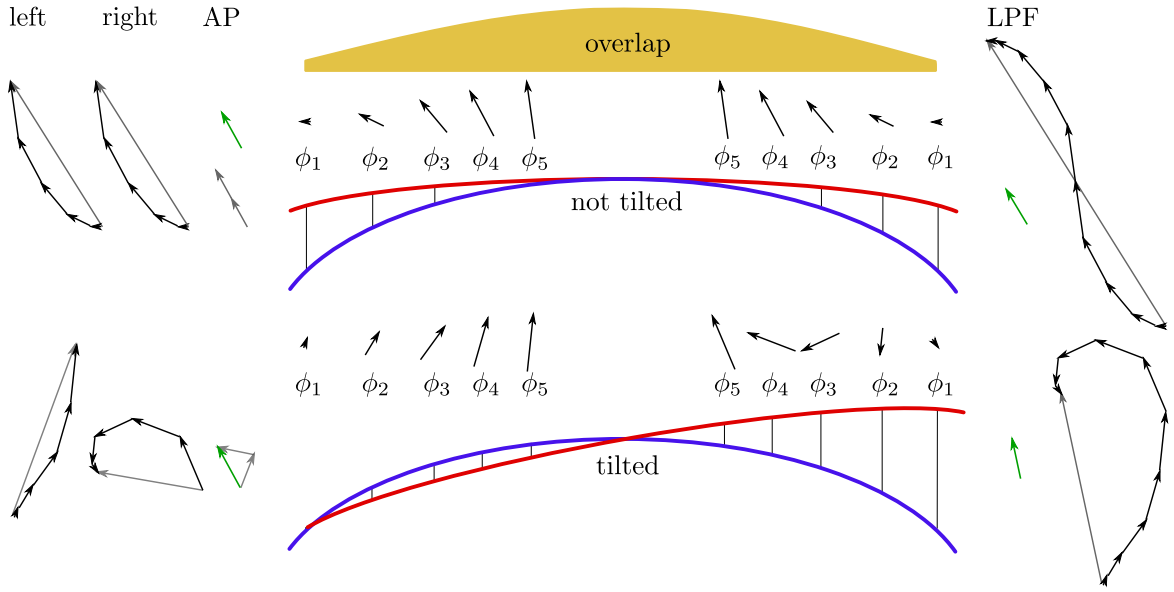

Figure 13. The effect of different path length definitions on the overall phase in case of unequal wavefront curvatures. On the right, the LPF path length signal is shown and on the left, the AP definition. Both, the LPF and the AP phases, change with the rotation. However, the AP phase is less affected by the tilts.

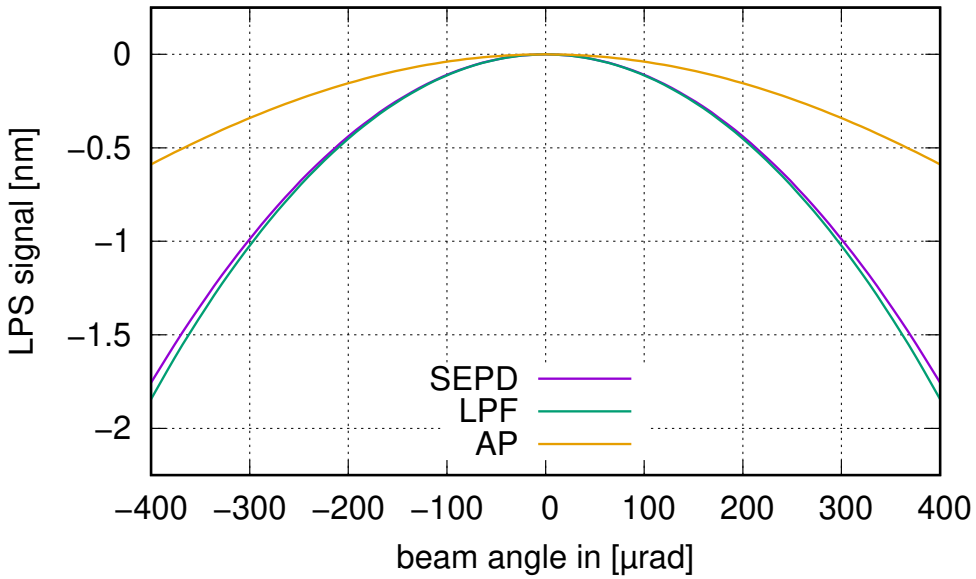

Figure 14. Longitudinal path length signals computed with IfoCAD for a single element diode, and for a QPD with either the LPF or the AP signal definition. Both beams are nominally equally aligned. One of the beams got tilted around its point of incidence ensuring a pure non-geometric signal. The simulation parameters were: waist radius w_{0r} =1 mm and w_{0r} =0.8 mm, distance from waist at detector $z_m = z_r = 100\,\mathrm{mm}$, pivot position $d_{\mathrm{long}} = d_{\mathrm{lat}} = 0\,\mathrm{mm}$, detector radius 5 mm, and slit width 50 μm.

whereby the notation $\int \mathrm{d}S\, f(x,y) = F(x,y)|_{\mathrm{PD}}$ describes the evaluation of the antiderivative $F(x,y)$ over the surface of the photodiode. If the photodiode surface consists of several segments, the notation describes the sum over these segments, inserting the boundary values respectively.

It can easily be verified that the second argument in Eq. (66) becomes zero for infinitely large SEPDs. Hence

$$\phi = \phi_{\mathrm{SEPD}} + \arg\left\{ \left[\frac{1}{4}\,\mathrm{erf}\left(\frac{C_x + C_{xx}\,x}{2\sqrt{C_{xx}}}\right)\right]\left[\frac{1}{4}\,\mathrm{erf}\left(\frac{C_y + C_{yy}\,y}{2\sqrt{C_{yy}}}\right)\right]\Big|_{\mathrm{PD}}\right\}. \tag{67}$$

We conclude that the phase measured for instance by a QPD is always the sum of the phase measured by an infinitely large SEPD and a second phase contribution that depends on the detector geometry. However, for large diodes with small deviations from SEPDs, as for example QPDs with a narrow insensitive slit, ϕ_{SEPD} will be the dominant summand. This agrees exactly with the simulation results shown in Fig. 14, where a QPD with a slit width of 50 μm was assumed and the $\mathrm{LPS}^{\mathrm{LPF}}$ signal deviates only slightly from the SEPD signal.

3.3.4. Arbitrary detector errors Like for arbitrary wavefront errors, also imperfections of the detector affect the TTL coupling. The segments can have different efficiencies or different shapes due to defects or additional features like bonding wires. Such disturbances are described and analysed for different detectors for instance in [29]. In such a case, the equations described throughout this paper would be disturbed by the imperfections and would, therefore, need to be adapted to the given situation. Naturally, we cannot adapt the given equations for arbitrary and unknown detector imperfections. Instead, we can say that arbitrary imperfections with no clear symmetry, could affect and change both the first- and second-order TTL contributions in the system or any other order of interest.

4. Summary non-geometric TTL coupling

In this section, we summarise the non-geometric TTL effects providing an estimate of the polynomial degree of the added TTL coupling. Throughout this paper, we have mostly assumed single element photodiodes, and therefore also assume this detector type here. However, we have shown in Sec. 3.3.3 that these results are relevant also when quadrant photodiodes are used, and that the deviation for QPDs and the $\mathrm{LPS}^{\mathrm{LPF}}$ signal from the given equations is particularly small. For simplicity, we assume here a nominally aligned measurement and reference beam, i.e. $\beta = 0$, $\varphi_r = 0$. Furthermore, we assume no detector tilt, i.e. $\varphi_{\mathrm{PD}} = 0$, since we have shown in Sec. 3.3.1 that the detector tilt angle cancels in either case from the total LPS signal.

Given two beams that are nominally aligned and always share the same point of incidence, the non-geometric coupling signal for equal beam parameters becomes negligible. However, we face TTL coupling if both beams feature different beam parameters (compare Eq. (52)), i.e.

$$\mathrm{LPS}_{\mathrm{ng}}^{\mathrm{SEPD,2D}} = -\left[\frac{(z_{Rr}^2+z_r^2)z_m-(z_{Rm}^2+z_m^2)z_r}{(z_{Rm}+z_{Rr})^2+(z_m-z_r)^2}\right]\frac{\varphi_m^2}{2}\,. \tag{68}$$

For equal and for unequal beam parameters, a static offset between the measurement and the reference beam ($x_{im} - x_{ir} = \text{const.}$) couples linearly into the signal. This holds for the case of a rotating setup as well as for a rotating mirror (compare Eq. (18)). Under our assumptions, we get for equal beam parameters

$$\mathrm{LPS}_{\mathrm{ng}}^{\mathrm{SEPD,2D}} \approx (x_{im}-x_{ir})\frac{\varphi_m}{2} \tag{69}$$

and for unequal beam parameters (compare Eq. (52))

$$\begin{aligned}&\mathrm{LPS}_{\mathrm{ng}}^{\mathrm{SEPD,2D}}\\ &\approx (x_{im}-x_{ir})\left[\frac{z_{Rm}(z_{Rm}+z_{Rr})+z_m(z_m-z_r)}{(z_{Rm}+z_{Rr})^2+(z_m-z_r)^2}\right]\varphi_m\\ &-\left[\frac{(z_{Rr}^2+z_r^2)z_m-(z_{Rm}^2+z_m^2)z_r}{(z_{Rm}+z_{Rr})^2+(z_m-z_r)^2}\right]\frac{\varphi_m^2}{2}\,.\end{aligned} \tag{70}$$

Furthermore, the TTL coupling in the case of a setup dependent beam walk, i.e. if the centre of rotation is not located on the photodiode surface, adds second-order TTL

coupling both for the case of angular jitter of the receiving system (RS, cf. Eq. (23)) or a reflecting mirror (MR, cf. Eq. (37)). We find for beams with equal beam parameters:

$$\mathrm{LPS}_{\mathrm{ng,RS}}^{\mathrm{SEPD,2D}}(\varphi_{\mathrm{RS}}(t)) \approx -\frac{1}{2}\, d_{\mathrm{long}}\, \varphi_{\mathrm{RS}}^2\,, \tag{71}$$

$$\mathrm{LPS}_{\mathrm{ng,MR}}^{\mathrm{SEPD,2D}}(\varphi(t)) \quad \approx\; -2 d_{\mathrm{lever}} \varphi^2\,. \tag{72}$$

Transmissive components also contribute as second-order TTL coupling, no matter whether angular jitter of a mirror or a receiving system is considered. For equal beam parameters we find (cf. Eq. (48)):

$$\begin{aligned}\mathrm{LPS}_{\mathrm{ng,tc}}^{\mathrm{SEPD,2D}} \approx \sum_i t_{\mathrm{BS},i} \Bigg[&\frac{n_{\mathrm{BS},i}^2 \cos(\varphi_{\mathrm{BS},i})^2}{(n_{\mathrm{BS},i}^2 - \sin^2(\varphi_{\mathrm{BS},i}))^{3/2}} - \frac{\sin^2(\varphi_{\mathrm{BS},i})}{\sqrt{n_{\mathrm{BS},i}^2 - \sin^2(\varphi_{\mathrm{BS},i})}} \\ &- \cos(\varphi_{\mathrm{BS},i}) \Bigg] \frac{\varphi_m^2}{2}\,. \end{aligned} \tag{73}$$

For non-equal beam parameters, we find not only second-order but also linear coupling since we get terms that depend on the static beam offsets and the dynamic beam walk. However, assuming a negligible static beam offsets, Eqs. (53), (54) and (55) reduce to second-order coupling equations.

$$\begin{aligned} &\mathrm{LPS}_{\mathrm{ng,RS}}^{\mathrm{SEPD,2D}}(\varphi_{\mathrm{RS}}(t)) \\ \approx\; &- d_{\mathrm{long}} \left[\frac{z_{Rm}(z_{Rm}+z_{Rr}) + z_m(z_m - z_r)}{(z_{Rm}+z_{Rr})^2 + (z_m - z_r)^2} \right] \varphi_{\mathrm{RS}}^2 \\ + \;&d_{\mathrm{long}}^2 \left[\frac{(z_m - z_r)}{2\left((z_{Rm}+z_{Rr})^2 + (z_m - z_r)^2\right)} \right] \varphi_{\mathrm{RS}}^2 \\ - \;&\left[\frac{(z_{Rr}^2 + z_r^2) z_m - (z_{Rm}^2 + z_m^2) z_r}{(z_{Rm}+z_{Rr})^2 + (z_m - z_r)^2} \right] \frac{\varphi_{\mathrm{RS}}^2}{2}\,, \end{aligned} \tag{74}$$

$$\begin{aligned} &\mathrm{LPS}_{\mathrm{ng,MR}}^{\mathrm{SEPD,2D}}(\varphi(t)) \\ \approx\; &- 4 d_{\mathrm{lever}} \left[\frac{z_{Rm}(z_{Rm}+z_{Rr}) + z_m(z_m - z_r)}{(z_{Rm}+z_{Rr})^2 + (z_m - z_r)^2} \right] \varphi^2 \\ + \;&2 d_{\mathrm{lever}}^2 \left[\frac{(z_m - z_r)}{(z_{Rm}+z_{Rr})^2 + (z_m - z_r)^2} \right] \varphi^2 \\ - \;&2 \left[\frac{(z_{Rr}^2 + z_r^2) z_m - (z_{Rm}^2 + z_m^2) z_r}{(z_{Rm}+z_{Rr})^2 + (z_m - z_r)^2} \right] \varphi^2\,, \end{aligned} \tag{75}$$

$$\begin{aligned} &\mathrm{LPS}_{\mathrm{ng,tc}}^{\mathrm{SEPD,2D}} \\ \approx\; &- \sum_i t_{\mathrm{BS},i} \left[\frac{n_{\mathrm{BS},i}^2 \cos(\varphi_{\mathrm{BS},i})^2}{(n_{\mathrm{BS},i}^2 - \sin^2(\varphi_{\mathrm{BS},i}))^{3/2}} - \frac{\sin^2(\varphi_{\mathrm{BS},i})}{\sqrt{n_{\mathrm{BS},i}^2 - \sin^2(\varphi_{\mathrm{BS},i})}} - \cos(\varphi_{\mathrm{BS},i}) \right] \\ &\cdot \left[\frac{z_{Rm}(z_{Rm}+z_{Rr}) + z_m(z_m - z_r)}{(z_{Rm}+z_{Rr})^2 + (z_m - z_r)^2} \right] \varphi_m^2 \end{aligned}$$

$$+\left(\sum_i t_{\mathrm{BS},i}\left[\frac{n_{\mathrm{BS},i}^2\cos(\varphi_{\mathrm{BS},i})^2}{(n_{\mathrm{BS},i}^2-\sin^2(\varphi_{\mathrm{BS},i}))^{3/2}}-\frac{\sin^2(\varphi_{\mathrm{BS},i})}{\sqrt{n_{\mathrm{BS},i}^2-\sin^2(\varphi_{\mathrm{BS},i})}}-\cos(\varphi_{\mathrm{BS},i})\right]\right)^2$$
$$\cdot\left[\frac{(z_m-z_r)}{(z_{Rm}+z_{Rr})^2+(z_m-z_r)^2}\right]\varphi_m^2$$
$$-\left[\frac{(z_{Rr}^2+z_r^2)z_m-(z_{Rm}^2+z_m^2)z_r}{(z_{Rm}+z_{Rr})^2+(z_m-z_r)^2}\right]\frac{\varphi_m^2}{2}\,. \tag{76}$$

Lateral jitter does not cause any first- or second-order non-geometric TTL coupling in the case of a jittering mirror and under the given assumptions:

$$\mathrm{LPS}_{\mathrm{ng,MR}}^{\mathrm{SEPD,2D}}(d_{\mathrm{lat}}(t))\approx 0\,. \tag{77}$$

However, this is different for a lateral jittering reference system. A laterally jittering receiving system changes the point of incidence of the measurement beam (x_{im}). Therefore, assuming a constant misalignment of the receiver with respect to the received beam and a varying point of incidence $x_{im}(t)$ of the latter, yields a strong linear TTL coupling for equal beam parameters by Eq. (28)

$$\mathrm{LPS}_{\mathrm{ng,RS}}^{\mathrm{SEPD,2D}}(y_{\mathrm{RS}}(t))\approx -\frac{1}{2}y_{\mathrm{RS}}(t)\,\varphi_{\mathrm{RS}} \tag{78}$$

as well as for unequal beam parameters

$$\mathrm{LPS}_{\mathrm{ng,RS}}^{\mathrm{SEPD,2D}}(y_{\mathrm{RS}}(t))$$
$$\approx -y_{\mathrm{RS}}(t)\left[\frac{z_{Rm}(z_{Rm}+z_{Rr})+z_m(z_m-z_r)}{(z_{Rm}+z_{Rr})^2+(z_m-z_r)^2}\right]\varphi_{\mathrm{RS}}\,. \tag{79}$$

For the given assumptions, all presented non-geometric TTL effects are summarised in Tab. 2. This table is the counterpart to the geometric TTL effects summarised in [1, cf Tab. 1].

5. Key findings on total TTL coupling

After summarising the non-geometric TTL effects in the previous section, we now discuss our findings on the total TTL effect, i.e. the sum of geometric and non-geometric TTL effects.

We have demonstrated in Secs. 3.2.3 - 3.2.5 that the total TTL coupling fully cancels if the centre of rotation lies on the beam's propagation axis, and the Gaussian beams have identical beam parameters. This holds also if transmissive components exist along the beam path. In either case, the beam walk induced non-geometric TTL coupling cancels the geometric TTL effects. However, if the centre of rotation is laterally shifted against the beam axis, the cancellation fails. Then, a significant geometric TTL coupling exists, that has no non-geometric counterpart.

We find an incomplete TTL cancellation in the case of unequal parameters. However, we can construct particular scenarios in which the cancellations holds again. If the interfering beams have an identical waist position and a pivot in the centre of the

Table 2. Overview of the different non-geometric cross-coupling mechanisms for a beam with normal incidence and no photodiode tilt (except where explicitly stated otherwise), i.e. $\beta = \varphi_{\mathrm{PD}} = 0$. We further assume normal incidence of the reference beam, i.e. $\varphi_r = 0$, and equal beam parameters, unless explicitly stated otherwise. For each effect we give a short description and the general behaviour (approximated), like linear, quadratic or mixed with respect to the tilt angle. Cross-coupling due to wavefront errors and detector geometry have in general an arbitrary form. The non-geometric effects apply both for mirror rotation (MR) or receiving system rotation (RS), unless explicitly mentioned otherwise.

		Cross-coupling mechanism	Name	General behaviour	Eq.	Sec.	Description
wavefront dependent TTL	lateral	receiver jiter	$\mathrm{LPS}^{\mathrm{SEPD}}_{\mathrm{ng,RS}}$	linear	(78),(79)	3.2.3	Lateral jitter yields a beam walk of the measurement beam.
		mirror jitter	$\mathrm{LPS}^{\mathrm{SEPD}}_{\mathrm{ng,MR}}$	negligible	(77)	3.2.4	Lateral jitter coupling affects the non-geometric LPS only at higher orders.
	angular	beam offset	$\mathrm{LPS}^{\mathrm{SEPD}}_{\mathrm{ng}}$	mixed	(69),(70)	3.2.2	Initial misalignment on the detector generates asymmetric disparity.
		beam walk					
		– receiver	$\mathrm{LPS}^{\mathrm{SEPD}}_{\mathrm{ng,RS}}$	quadratic	(71),(74)	3.2.3	Offsets between rotation point and detector lead to angle dependent beam walk.
		– mirror	$\mathrm{LPS}^{\mathrm{SEPD}}_{\mathrm{ng,MR}}$	quadratic	(72),(75)	3.2.4	Same as for RS beam walk.
		– transmissive components	$\mathrm{LPS}^{\mathrm{SEPD}}_{\mathrm{ng,tc}}$	quadratic	(73),(76)	3.2.5	Transmissive optical components lead to an additional angle dependent beam walk.
		beam parameters	$\mathrm{LPS}^{\mathrm{SEPD}}_{\mathrm{ng}}$	quadratic	(68)	3.2.6	Tilting wavefronts with a curvature mismatch generates coupling.
	both	reference beam tilt		linear		3	Reference beam tilts add in all cases linear coupling.
		wavefront errors		arbitrary		3.2.7	Aberrations in the wavefronts disturb the balance between different detector sides.
detector TTL	both	detector geometry		arbitrary		3.3.4	Errors and additional detector features alter the measured results.
		tilt of detector		negligible	(59)	3.3.1	Tilting the detector effects the geometric and non-geometric cross-coupling inversely. Hence its contribution to the full signal cancels.

waist, the geometric and the non-geometric signal cancel despite a possible arbitrary waist size mismatch, see Sec. 3.2.6.

With a dedicated lens system, one can image the centre of rotation of the beam onto its point of incidence at the detector [27, 11]. In this case, we find no geometric TTL coupling but non-geometric coupling terms due to the wavefront inequalities of the two beams. If imaging the point of rotation not exactly onto the detector surface or shifting the photodiode longitudinally, a small geometric coupling remains, which can for a suitable alignment counteract the non-geometric coupling [2]. Therefore, such imaging systems can significantly suppress the observed TTL coupling and will be used for this purpose in the LISA mission (e.g. [2]).

Another case of non-geometric TTL coupling without a geometric counterpart can be found if the points of incidence of the two beams do not coincide but have a static offset. We show in Sec. 3.2.2 that this offset breaks the wavefront symmetry even for equal beam parameters and generates linear non-geometric TTL coupling. Thus, an intentional offset of one of the beams can counteract other linear TTL coupling effects without simultaneously changing the geometric TTL coupling.

Analogously, lateral jitter of the receiving system effectively changes the offset between the two beams at the detector without changing their geometric path length. The resulting total lateral jitter coupling originates from non-geometric effects only, and is linear (Sec. 3.2.3).

This is different for the lateral jitter of a test mass, where the test mass moves into or out of the beam path. This shortens or elongates the beams' optical path length. On the other hand, the lateral jitter induces only negligible non-geometric TTL coupling effects since the reflected beam neither tilts nor significantly shifts in a lateral direction (Sec. 3.2.4).

For both considered systems, a lateral offset between the centre of rotation and the point of reflection (angular test mass jitter) or point of detection (angular receiver jitter), respectively, induces linear TTL coupling [1]. This coupling is fully geometric since any non-geometric signal contributions are negligible, see Secs. 3.2.3 and 3.2.4. Therefore, applying a lateral shift of the respective centre of rotation can be used to counteract other linear angular TTL coupling effects.

In summary, these presented TTL mechanisms can be used to counteract the overall TTL coupling even if the single underlying effects are unknown. This has been proven efficient in experiments (e.g. [11, 2, 30]).

6. Conclusion

Throughout this work, we have described TTL coupling as the angular and lateral motion of a mirror reflecting one of the interfered beams, or the jitter of a receiving system with respect to a received beam, coupling into the phase readout. This coupling adds unwanted noise to the phase signal. The TTL coupling noise is an important noise source in precision interferometers, particularly in space interferometers, such as

future space-based gravitational wave observatories like LISA, or the geodesy mission GRACE-FO and its successors. In this work we categorised the different non-geometric TTL coupling mechanisms for the interference of two Gaussian beams. We distinguish between the effects originating from the characteristics of the wavefronts, and the detector geometry including different path length signal definitions.

Wherever possible, we computed these non-geometric effects analytically from the overlap integral over the beams' electrical fields. The results agree with the numeric computations done by the simulation tool IfoCAD.

We summarised our key findings of the various non-geometric TTL coupling effects in Sec. 4 and Tab. 2. Additionally, we combined these key findings with the geometric TTL results presented in [1] to estimate the total TTL coupling. In Sec. 5, we discussed in which cases the geometric and non-geometric TTL mechanisms cancel each other, or can intentionally be used to counteract other TTL effects for minimising the total TTL coupling.

Our findings can be a valuable tool for the suppression of TTL coupling noise either by design or realignment in an existing system. Such a suppression is essential for a reduction of the TTL noise to a magnitude that can finally be removed by subtraction in post-processing [13, 31].

Acknowledgments

This work was made possible by funds of both the Deutsche Forschungsgemeinschaft (DFG) and the German Space Agency, DLR. We gratefully acknowledge the Deutsche Forschungsgemeinschaft (DFG) for funding the Sonderforschungsbereich (SFB 1128: geo-Q) "Relativistic Geodesy and Gravimetry with Quantum Sensors", project A05 and all work contributions to this paper made by Sönke Schuster. Furthermore, we acknowledge DFG for funding the Clusters of Excellence PhoenixD (EXC 2122, Project ID 390833453) and QuantumFrontiers (EXC 2123, Project ID 390837967). Likewise, we gratefully acknowledge the German Space Agency, DLR and support by the Federal Ministry for Economic Affairs and Energy based on a resolution of the German Bundestag (FKZ 50OQ1801). Finally, we would like to acknowledge the Max Planck Society (MPG) for supporting the framework LEGACY on low-frequency gravitational wave astronomy, a cooperation between the Chinese Academy of Sciences (CAS) and the MPG (M.IF.A.QOP18098).

References

[1] MS Hartig, S Schuster, and G Wanner. Geometric tilt-to-length coupling in precision interferometry: mechanisms and analytical descriptions. *Journal of Optics*, 24(6):065601, may 2022.

[2] M. Chwalla, K. Danzmann, M. Dovale Álvarez, J.J. Esteban Delgado, G. Fernández Barranco, E. Fitzsimons, O. Gerberding, G. Heinzel, C.J. Killow, M. Lieser, M. Perreur-Lloyd, D.I. Robertson, J.M. Rohr, S. Schuster, T.S. Schwarze, M. Tröbs, G. Wanner, and H. Ward. Optical

suppression of tilt-to-length coupling in the lisa long-arm interferometer. *Phys. Rev. Applied*, 14:014030, Jul 2020.

[3] G Wanner, G Heinzel, E Kochkina, C Mahrdt, B Sheard, S Schuster, and K Danzmann. Methods for simulating the readout of lengths and angles in laser interferometers with gaussian beams. *Optics communications*, 285(24):4831–4839, 2012.

[4] P. Amaro-Seoane, H. Audley, S. Babak, J. Baker, E. Barausse, P. Bender, E. Berti, P. Binetruy, M. Born, D. Bortoluzzi, J. Camp, C. Caprini, V. Cardoso, M. Colpi, J. Conklin, N. Cornish, C. Cutler, K. Danzmann, R. Dolesi, L. Ferraioli, V. Ferroni, E. Fitzsimons, J. Gair, L. Gesa Bote, D. Giardini, F. Gibert, C. Grimani, H. Halloin, G. Heinzel, T. Hertog, M. Hewitson, K. Holley-Bockelmann, D. Hollington, M. Hueller, H. Inchauspe, P. Jetzer, N. Karnesis, C. Killow, A. Klein, B. Klipstein, N. Korsakova, S. L Larson, J. Livas, I. Lloro, N. Man, D. Mance, J. Mo, I. Mateos, K. McKenzie, S. T McWilliams, C. Miller, G. Mueller, G. Nardini, G. Nelemans, M. Nofrarias, A. Petiteau, P. Pivato, E. Plagnol, E. Porter, J. Reiche, D. Robertson, N. Robertson, E. Rossi, G. Russano, B. Schutz, A. Sesana, D. Shoemaker, J. Slutsky, C. F. Sopuerta, T. Sumner, N. Tamanini, I. Thorpe, M. Troebs, M. Vallisneri, A. Vecchio, D. Vetrugno, S. Vitale, M. Volonteri, G. Wanner, H. Ward, P. Wass, W. Weber, J. Ziemer, and P. Zweifel. Laser Interferometer Space Antenna. *ArXiv e-prints*, February 2017.

[5] O Jennrich. LISA technology and instrumentation. *Classical and Quantum Gravity*, 26(15):153001, jul 2009.

[6] M Chwalla, K Danzmann, GF Barranco, E Fitzsimons, O Gerberding, G Heinzel, C J Killow, M Lieser, M Perreur-Lloyd, D I Robertson, S Schuster, T Schwarze, M Tröbs, H Ward, and M Zwetz. Design and construction of an optical test bed for LISA imaging systems and tilt-to-length coupling. *Classical and Quantum Gravity*, 33(24):245015, 2016.

[7] C P Sasso, G Mana, and S Mottini. Coupling of wavefront errors and pointing jitter in the LISA interferometer: misalignment of the interfering wavefronts. *Classical and Quantum Gravity*, 35(24):245002, nov 2018.

[8] C P Sasso, G Mana, and S Mottini. Coupling of wavefront errors and jitter in the LISA interferometer: far-field propagation. *Classical and Quantum Gravity*, 35(18):185013, aug 2018.

[9] C P Sasso, G Mana, and S Mottini. Telescope jitters and phase noise in the lisa interferometer. *Opt. Express*, 27(12):16855–16870, Jun 2019.

[10] S Schuster, G Wanner, M Tröbs, and G Heinzel. Vanishing tilt-to-length coupling for a singular case in two-beam laser interferometers with gaussian beams. *Applied optics*, 54(5):1010–1014, 2015.

[11] M Tröbs, S Schuster, M Lieser, M Zwetz, M Chwalla, K Danzmann, GF Barránco, E Fitzsimons, O Gerberding, G Heinzel, C Killow, M Perreur-Lloyd, D Robertson, T Schwarze, G Wanner, and H Ward. Reducing tilt-to-length coupling for the lisa test mass interferometer. *Classical and Quantum Gravity*, 35(10):105001, apr 2018.

[12] H Wegener, V Müller, G Heinzel, and M Misfeldt. Tilt-to-length coupling in the grace follow-on laser ranging interferometer. *Journal of Spacecraft and Rockets*, 57(6):1362–1372, 2020.

[13] M Armano, H Audley, G Auger, JT Baird, M Bassan, P Binetruy, M Born, D Bortoluzzi, N Brandt, M Caleno, et al. Sub-femto-g free fall for space-based gravitational wave observatories: Lisa pathfinder results. *Physical Review Letters*, 116(23):231101, 2016.

[14] G Wanner, N Karnesis, and LISA Pathfinder collaboration. Preliminary results on the suppression of sensing cross-talk in lisa pathfinder. *Journal of Physics: Conference Series*, 840(1):012043, 2017.

[15] M. Armano, H. Audley, J. Baird, P. Binetruy, M. Born, D. Bortoluzzi, E. Castelli, A. Cavalleri, A. Cesarini, A. M. Cruise, K. Danzmann, M. de Deus Silva, I. Diepholz, G. Dixon, R. Dolesi, L. Ferraioli, V. Ferroni, E. D. Fitzsimons, M. Freschi, L. Gesa, F. Gibert, D. Giardini, R. Giusteri, C. Grimani, J. Grzymisch, I. Harrison, G. Heinzel, M. Hewitson, D. Hollington, D. Hoyland, M. Hueller, H. Inchauspé, O. Jennrich, P. Jetzer, N. Karnesis, B. Kaune, N. Korsakova, C. J. Killow, J. A. Lobo, I. Lloro, L. Liu, J. P. López-Zaragoza,

R. Maarschalkerweerd, D. Mance, N. Meshksar, V. Martín, L. M-Polo, J. Mo, F. M-Porqueras, I. Mateos, P. W. McNamara, J. Mendes, L. Mendes, M. Nofrarias, S. Paczkowski, M. Perreur-Lloyd, A. Petiteau, P. Pivato, E. Plagnol, J. Ramos-Castro, J. Reiche, D. I. Robertson, F. Rivas, G. Russano, J. Slutsky, C. F. Sopuerta, T. Sumner, D. Texier, J. I. Thorpe, D. Vetrugno, S. Vitale, G. Wanner, H. Ward, P. Wass, W. J. Weber, L. Wissel, A. Wittchen, and P. Zweifel. Calibrating the system dynamics of lisa pathfinder. *Phys. Rev. D*, 97:122002, Jun 2018.

[16] M. Armano, H. Audley, J. Baird, P. Binetruy, M. Born, D. Bortoluzzi, E. Castelli, A. Cavalleri, A. Cesarini, A. M. Cruise, K. Danzmann, M. de Deus Silva, I. Diepholz, G. Dixon, R. Dolesi, L. Ferraioli, V. Ferroni, E. D. Fitzsimons, M. Freschi, L. Gesa, F. Gibert, D. Giardini, R. Giusteri, C. Grimani, J. Grzymisch, I. Harrison, G. Heinzel, M. Hewitson, D. Hollington, D. Hoyland, M. Hueller, H. Inchauspé, O. Jennrich, P. Jetzer, N. Karnesis, B. Kaune, N. Korsakova, C. J. Killow, J. A. Lobo, I. Lloro, L. Liu, J. P. López-Zaragoza, R. Maarschalkerweerd, D. Mance, N. Meshksar, V. Martín, L. M-Polo, J. Mo, F. M-Porqueras, I. Mateos, P. W. McNamara, J. Mendes, L. Mendes, M. Nofrarias, S. Paczkowski, M. Perreur-Lloyd, A. Petiteau, P. Pivato, E. Plagnol, J. Ramos-Castro, J. Reiche, D. I. Robertson, F. Rivas, G. Russano, J. Slutsky, C. F. Sopuerta, T. Sumner, D. Texier, J. I. Thorpe, D. Vetrugno, S. Vitale, G. Wanner, H. Ward, P. Wass, W. J. Weber, L. Wissel, A. Wittchen, and P. Zweifel. Lisa pathfinder, 2019.

[17] P McNamara, S Vitale, K Danzmann, LISA Pathfinder Science Working Team, et al. Lisa pathfinder. *Classical and Quantum Gravity*, 25(11):114034, 2008.

[18] BS Sheard, G Heinzel, K Danzmann, DA Shaddock, WM Klipstein, and WM Folkner. Intersatellite laser ranging instrument for the grace follow-on mission. *Journal of Geodesy*, 86(12):1083–1095, 2012.

[19] K Abich, A Abramovici, B Amparan, A Baatzsch, B Okihiro, D Barr, M Bize, C Bogan, C Braxmaier, M Burke, K Clark, C Dahl, K Dahl, K Danzmann, M Davis, G de Vine, J Dickson, S Dubovitsky, A Eckardt, T Ester, GF Barranco, R Flatscher, F Flechtner, W Folkner, S Francis, M Gilbert, F Gilles, M Gohlke, N Grossard, B Guenther, P Hager, J Hauden, F Heine, G Heinzel, M Herding, M Hinz, J Howell, M Katsumura, M Kaufer, W Klipstein, A Koch, M Kruger, K Larsen, A Lebeda, A Lebeda, T Leikert, C Liebe, J Liu, L Lobmeyer, C Mahrdt, T Mangoldt, K McKenzie, M Misfeldt, P Morton, V Müller, A Murray, D Nguyen, K Nicklaus, R Pierce, J Ravich, G Reavis, J Reiche, J Sanjuan, D Schütze, C Seiter, D Shaddock, B Sheard, M Sileo, R Spero, G Spiers, G Stede, M Stephens, A Sutton, J Trinh, K Voss, D Wang, R Wang, B Ware, H Wegener, S Windisch, C Woodruff, B Zender, and M Zimmermann. In-orbit performance of the grace follow-on laser ranging interferometer. *Phys. Rev. Lett.*, 123:031101, Jul 2019.

[20] E Kochkina, G Heinzel, G Wanner, V Müller, C Mahrdt, B Sheard, S Schuster, and K Danzmann. Simulating and optimizing laser interferometers. *9th LISA Symposium*, pages 291–292, 2013.

[21] G Wanner and G Heinzel. Analytical description of interference between two misaligned and mismatched complete gaussian beams. *Applied optics*, 53(14):3043–3048, 2014.

[22] S Schuster, M Tröbs, G Wanner, and G Heinzel. Experimental demonstration of reduced tilt-to-length coupling by a two-lens imaging system. *Optics Express*, 24(10):10466–10475, 2016.

[23] E Morrison, B Meers, D Robertson, and H Ward. Automatic alignment of optical interferometers. *Applied Optics*, 33(22), 1994.

[24] G Wanner, S Schuster, M Tröbs, and G Heinzel. A brief comparison of optical pathlength difference and various definitions for the interferometric phase. *Journal of Physics: Conference Series*, 610:012043, 2015.

[25] Gerhard Heinzel, Miguel Dovale Álvarez, Alvise Pizzella, Nils Brause, and Juan José Esteban Delgado. Tracking length and differential-wavefront-sensing signals from quadrant photodiodes in heterodyne interferometers with digital phase-locked-loop readout. *Phys. Rev. Applied*, 14:054013, Nov 2020.

[26] G Heinzel, C Braxmaier, R Schilling, A Rüdiger, D Robertson, M Te Plate, V Wand, K Arai, U Johann, and K Danzmann. Interferometry for the lisa technology package (ltp) aboard

smart-2. *Classical and Quantum Gravity*, 20(10):S153, 2003.

[27] S Schuster. *Tilt-to-length coupling and diffraction aspects in satellite interferometry*. PhD thesis, Leibniz Universität Hannover, 2017.

[28] J. Bogenstahl, C. Diekmann, E. Granova, T. Schwarze, M. Tröbs, and G. Wanner. Optical bench EBB design definition file - opto-electronics & alternative beam compressors. Technical Report LOB-AEI-TN-008.1-08, AEI, 06 2011.

[29] GF Barranco, M Tröbs, V Müller, O Gerberding, F Seifert, and G Heinzel. Spatially resolved photodiode response for simulating precise interferometers. *Applied Optics*, 55(24):6688–6693, 2016.

[30] Y Lee. *Development of an advanced tilt actuator for tilt-to-length coupling investigations*. PhD thesis, Leibniz Universität Hannover, 2021.

[31] R Giusteri, S Paczkowski, M Hewitson, N Karnesis, and E D Fitzsimons. Post-processing subtraction of tilt-to-length noise in LISA. *In preparation*, 2022.